2003

On the influence of fault bends on the growth of sub-Rayleigh and intersonic dynamic shear ruptures

Carl-Ernst Rousseau
University of Rhode Island, roussce@uri.edu

Ares J. Rosakis

Citation/Publisher Attribution

Rousseau, C.-E., and A. J. Rosakis (2003), On the influence of fault bends on the growth of sub-Rayleigh and intersonic dynamic shear ruptures, *J. Geophys. Res.*, 108, 2411, doi: 10.1029/2002JB002310, B9.
Available at: https://doi.org/10.1029/2002JB002310

On the influence of fault bends on the growth of sub-Rayleigh and intersonic dynamic shear ruptures

JOURNAL OF GEOPHYSICAL RESEARCH, VOL. 108, NO. B9, 2411, doi:10.1029/2002JB002310, 2003

On the influence of fault bends on the growth of sub-Rayleigh and intersonic dynamic shear ruptures

Carl-Ernst Rousseau[1]
Department of Mechanical Engineering, University of Rhode Island, Kingston, Rhode Island, USA

Ares J. Rosakis
Graduate Aeronautical Laboratories, California Institute of Technology, Pasadena, California, USA

Received 15 November 2002; revised 27 March 2003; accepted 19 June 2003; published 4 September 2003.

[1] Earthquake ruptures are modeled as dynamically propagating shear cracks with the aim of gaining insight into the physical mechanisms governing their arrest or, otherwise, the often-observed variations in rupture speeds. Fault bends have been proposed as being the main cause for these variations. Following this line of reasoning, the existence of deviations from fault planarity is chosen as the main focus of this study. Asymmetric impact is used to generate shear loading and to propagate dynamic mode-II cracks along the bonded interfaces of two otherwise identical homogeneous constituents. Secondary paths inclined at various angles are also introduced to represent fault bends or kinks. The experiments show that certain fault bend inclinations are favored as alternate paths for rupture continuation, whereas others suppress further motion of the incoming rupture. The asymptotic elastodynamic stress fields at the tip of the growing rupture are used to develop two criteria (one energetic and one stress based) for rupture propagation or arrest at the kinked interfaces. These criteria correlate very well with the experimental results. Since most field evidence suggests that the average rupture speeds during crustal earthquakes are sub-Rayleigh, this work first focuses on incoming rupture speeds that are just below the Rayleigh wave speed. Reports of intersonic crustal fault rupture speeds having surfaced recently, experiments and analyses are also performed within that speed regime. *INDEX TERMS:* 7209 Seismology: Earthquake dynamics and mechanics; 7203 Seismology: Body wave propagation; 7260 Seismology: Theory and modeling; 8010 Structural Geology: Fractures and faults; 8020 Structural Geology: Mechanics; *KEYWORDS:* shear crack, wave propagation, dynamic fracture, fault bend, energy release rate, fault propagation criteria

Citation: Rousseau, C.-E., and A. J. Rosakis, On the influence of fault bends on the growth of sub-Rayleigh and intersonic dynamic shear ruptures, *J. Geophys. Res.*, *108*(B9), 2411, doi:10.1029/2002JB002310, 2003.

1. Introduction

[2] Earthquakes generally result from a sudden rupture in the Earth's crust, which occurs under the influence of slowly increasing compressive and shear tectonic stresses. Nucleation and propagation of such events take place along preexisting faults in the Earth's crust. However, these weak paths are rarely planar but rather exhibit kinks, discontinuities, jogs, and varying levels of strength, which assume a great importance in seismology. For example, branches and steps are believed to control the extent to which earthquake ruptures are able to propagate, thereby potentially restricting their magnitude. *King and Nabelek* [1985], in particular, have noted the apparent confinement of earthquakes to regions between fault bends, and in a few cases, have isolated their initiation to the immediate vicinity of bends or jogs. Arrest at those locations, however, is not an inevitable outcome. Indeed, earthquakes have in some cases been observed to bypass geometrical discontinuities. For example, the 1966 Parkfield earthquake jumped across a step over in the San Andreas fault [*Segall and Du*, 1993].

[3] The impact of fault kinks on overall earthquake progression, though acknowledged, has rarely undergone rigorous scrutiny to the extent that jogs have. This arises from the difficulty that exists in quantifying their role. Thus far, the most advanced analysis on the subject is due to *Poliakov et al.* [2002] who have approached the problem from two different angles. Successively, the propagating earthquake is likened to a steadily propagating and singular elastodynamic shear crack and is then represented by a slip-weakening dynamic rupture model. Off-fault maximum shear stresses in the vicinity of the propagating tip are evaluated and compared to the frictional resistance within the Earth's crust. When the former exceeds the latter in a particular direction, that direction becomes a plane of potential failure. In cases where extensive damage is

---

[1] Also at Graduate Aeronautical Laboratories, California Institute of Technology, Pasadena, California, USA.

0148-0227/03/2002JB002310$09.00

present, this results in secondary faulting. They also find that were an intersecting weak plane aligned to that direction, this plane would then promptly rupture. In addition to the nature of the local field of the incoming rupture, their results are highly dependent upon the level of tectonic stress. Further, *Aochi et al.* [2002] and *Kame et al.* [2003] have studied the effect of these stresses on symmetric and asymmetric forked fault geometries with the aid of numerical analysis. Depending on tectonic stress level, orientation, and incoming rupture speed, the rupture may favor the more compressional or the more tensional of the tectonic branches.

[4] In this work, a close analogy between earthquakes and cracks will be embraced. The traditional engineering approach to fracture mechanics has been primarily guided by opening (mode-I) cracks, largely neglecting shear (mode-II) cracks. This is indeed very practical as crack propagation in constitutively homogeneous, monolithic materials is strictly limited to the opening mode, even if far-field conditions are asymmetric. As a crack extends under the influence of external tractions, it will continually kink and assume a local mode-I field, even if the external tractions are such as to generate mixed-mode stress states [*Cotterell and Rice*, 1980]. Seismologists, on the other hand, face different concerns. The Earth's crust inherently contains numerous weak interfaces, or faults, and therefore from a fracture standpoint can no longer be construed as monolithic. In addition, active faulting brings into frictional contact rocks that are compositionally dissimilar, thereby inducing material inhomogeneity. In some cases, elastic material properties across several faults have been found to vary substantially, and shear wave speeds have been measured to differ by as much as 30% [*Das*, 1985; *Rice*, 2001]. The latter case simply constitutes a bimaterial with a weaker interface fracture toughness than either of its two constituents. Bimaterial cracks have a natural affinity toward acquiring a mixed-mode stress state, and even purely tensile external tractions generate a substantial mode-II component at the crack tip, due to the influence of material inhomogeneity. Also, the fault represents a ready-made path along which the rupture propagation is constrained. Thus the running rupture is prevented from kinking and thus is disallowed the opportunity of assuming pure mode I.

[5] The different crack-tip running modes and the presence or absence of weak paths also translate in differences in attainable crack speeds. Dynamically propagating tensile cracks are theoretically limited to c_R, the Rayleigh wave speed of the material [*Freund*, 1990]. However, in brittle monolithic materials, mode-I cracks can propagate smoothly only up to nearly 40% of c_R, at which point they become unstable, generating microbranches and engaging into tortuous paths [*Ramulu and Kobayashi*, 1985]. However, the introduction of a weak path in an otherwise homogeneous solid does set the environment for propagation of mode-I crack at its theoretical speed limit. For dynamic, mode-II, shear ruptures, the situation is very different. Here the existence of a weak plane or fault is a prerequisite for the existence of dynamic shear rupture of any speed. In contrast to their mode-I counterparts, mode-II cracks (or shear ruptures) propagating along faults are not only allowed to reach c_R theoretically but also are capable of jumping that barrier to reach the intersonic region between the shear wave speed (c_s) and the longitudinal wave speed (c_l) [*Burridge et al.*, 1979]. Field observations seem to confine the rupture speed of most earthquakes to the range between $0.7c_s$ ($0.76c_R$) and $0.9c_s$ ($0.98c_R$) [*Kanamori*, 1994]. In only very few cases have earthquake rupture speeds been inferred to have become intersonic over a limited portion of the fault [*Archuleta*, 1984; *Olsen et al.*, 1997; *Bouchon et al.*, 2001].

[6] Of particular interest to the present investigation is the rupture event that occurred along the North Anatolian fault during the 1999 Izmit earthquake. In this event, *Bouchon et al.* [2001] present compelling evidence that the east bound rupture propagated intersonically with a speed just above $\sqrt{2}c_s$, while the west bound rupture remained sub-Rayleigh. Partially confirming these results are the more recent numerical evaluations of R. A. Harris (personal communication, 2002) that require the existence of supershear speeds as a necessary condition for complete rupture of the North Anatolian fault. The intersonic east bound rupture encountered a 22.5°-retaining bend in the fault (compression side) that was unable to stop the rupture (see analysis by *Harris et al.* [2002]). Situations mimicking such an encounter of an intersonic rupture with a compression bend will be discussed in the second part of this study.

[7] Despite the caution in claiming the existence of intersonic earthquake ruptures, strong evidence of intersonic crack propagation has surfaced recently in laboratory settings. *Lambros and Rosakis* [1995] have witnessed a number of cases in which intersonic speeds were attained along the bonded interface between two highly dissimilar materials. This was further discussed in the review paper by *Singh et al.* [1997]. Even more notable is the discovery of bonded identical materials sustaining propagating crack speeds in the intersonic regime [*Rosakis et al.*, 1999], which certainly adds credence to the possibility of intersonic earthquake rupture.

[8] The above discussion has raised several issues pertinent to dynamic rupture propagation in the Earth's crust. It was shown that the reasons for the initiation and the arrest of ruptures remain evasive. Using experimental techniques of dynamic fracture mechanics, this paper aims at partially answering the second question. Indeed, relations are developed that correlate the presence of fault bends to variations in the speed of the propagating rupture. However, certain limitations are associated with the present methodology. For instance, earthquake ruptures are resisted mainly by friction, which in this case is simulated by an interfacial bond strength. Also, in the present work, rupture is triggered by impact, whereas in earthquake ruptures they are excited by slow crustal motion and the resulting tectonic loading as well as the sudden release of local pressure. Above all, this work presents some valid conceptual answers which should universally apply to the rupture of a weak bond by a propagating crack as well as the overcoming of fault friction by a propagating earthquake rupture.

[9] In the following, specimens and experimental setup are described. Results of the experiments are then presented, and the analytical basis of this work is developed. Finally, the experimental results are discussed in view of two different failure criteria. The outline hereby laid out for the case of sub-Rayleigh cracks is then repeated for the

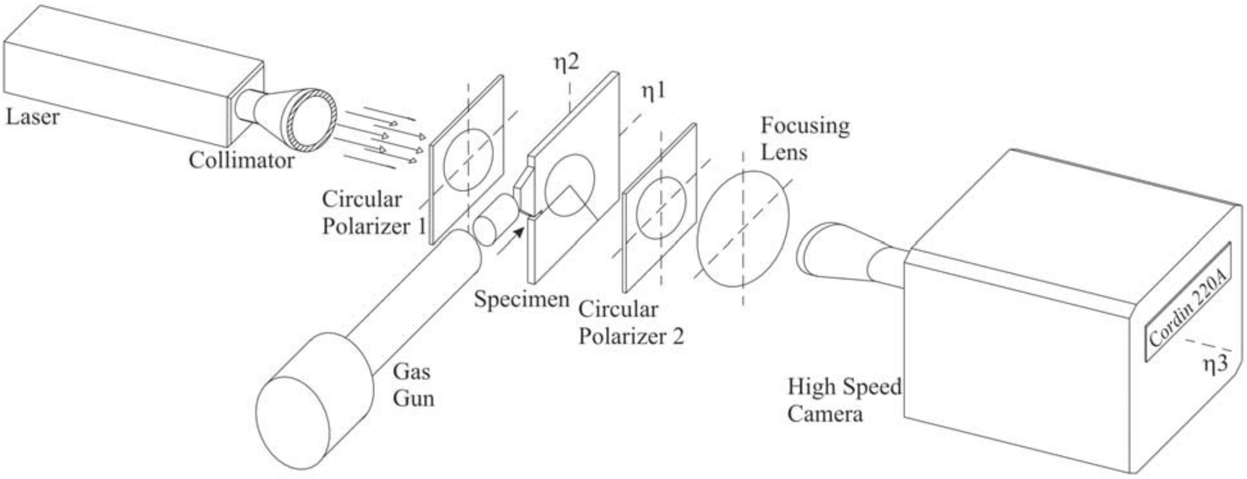

Figure 1. The dynamic photoelastic setup and the high-speed camera.

intersonic case, as it is believed here that earthquake ruptures have the potential of running intersonically.

2. Specimen Description and Experimental Apparatus

[10] The study investigates the progression, transmission, or arrest behavior of shear-dominated sub-Rayleigh and intersonic cracks growing along weak paths, as these ruptures encounter fault bends or kinks along their paths. The optical method of photoelasticity is used as a means of visualizing stress fields in real time. The method lends itself particularly well to revealing the essential features of intersonic cracks, such as shear shock waves, and will therefore be used in both cases. In addition, this full-field technique also relates stress field information around propagating cracks. The events are recorded using high-speed photography.

[11] The specimens were composed of Homalite-100, a birefringent polymer with longitudinal, shear, and Rayleigh wave speeds of c_l = 2295 m s^{-1}, c_s = 1310 m s^{-1}, and c_R = 1205 m s^{-1}, respectively. At room temperature and at strain rates prevailing during the experiments (10^3 s^{-1}), the material is extremely brittle and linear elastic.

[12] The specimens were 5 mm thick, 175 mm high, and 200 mm long. The narrowness of the specimens ensured the prevalence of two-dimensional, generalized plane stress conditions. Preferred paths were generated by machining them, beginning halfway through the specimen height on the left side, and following the prescribed route. The two halves were then bonded with a solution having weakened fracture properties with respect to the bulk material but similar elastic properties and density, as measured by *Samudrala et al.* [2002a]. The weaker adhesive joint traps the moving crack to the prescribed interface, compelling it to retain its originally imposed mode-II state. Although not monolithic, the resulting specimens can be considered to be constitutively homogeneous. Indeed, the existence of a path of lower fracture toughness makes these specimens fracture-wise inhomogeneous but does not, in any sense, affect their continuum mechanics description. Along the interface, a 15-mm-long and 1-mm-wide starter notch was machined. The presence of the notch prevented the immediate transmission of the incoming impact stress waves (applied at the top) to the bottom half. This in turn guaranteed a relatively clean mode-II initiation loading of the notch tip by preventing notch face contact. The kinks in the weak path were placed 75 mm from the left edge. Placement of these alternate paths away from the loading (left edge) of the plate allowed the incoming crack to establish a steady state speed before reaching the bend site, thereby ensuring uniform conditions at the intersection of the two paths. Also, the location of the bend was even farther away from the distant right edge. The specimens were thus designed so that reflected longitudinal waves returning from that edge would not reach the location of the bend until the crack would have moved through the major portion of the alternate path, well beyond the experimental field of observation.

[13] The photoelastic setup is sketched in Figure 1. It consists of a collimated beam generated by an argon-ion continuous laser that is transmitted through a circular polarizer, the specimen, and a second circular polarizer. The information is directed to the iris of a digital high-speed Cordin camera capable of recording 16 frames up to a rate nearing 100 million frames per second. This time resolution is fortuitous, as very high crack speeds are present in some cases encountered here.

3. Experimental Observations in the Subsonic Regime

[14] Loading was generated by impact of a steel buffer bonded to the top half of the specimen, near the notch, by a hardened steel projectile. Following impact, an initially planar compressive wave is transmitted to the specimen via the steel buffer. Over the length of the notch, only the top portion of the specimen is loaded. Beyond that location, the compressive wave is gradually transmitted to the bottom. As a result, loading to the latter always lags that of the top. A state of stress thus exists along the interface, wherein a larger amount of shear and compression continually prevails above the adhesive joint. The condition is therefore propitious to crack initiation at the notch tip in a combination of compression and mode II, followed by propagation of a

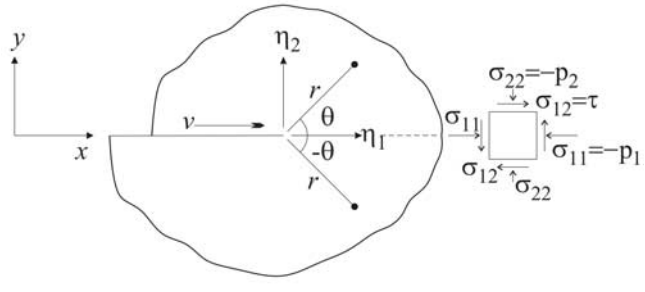

Figure 2. Schematic defining coordinate system convention and the initial state of stress ahead of the growing rupture.

shearing crack, in a manner similar to the stress state presented in the sketch of Figure 2. In addition, since the specimens are impacted on the top half, from left to right, the current experiments are akin to cases where earthquake ruptures feature right-lateral slip.

[15] Further, a coordinate system (η_1, η_2), moving with the crack tip is defined in Figure 2. The origin of the stationary prenotch is located at (x, y) and is related to the moving crack-tip location by $\eta_1 = x - \int_0^t v(t')dt'$ and $\eta_2 = y$. In addition, angular conventions are presented, with positive angles situated above the fault line (counterclockwise) and negative angles situated below the fault line (clockwise). This angular convention is carried over to the specimen geometry, as secondary bend paths are placed at various angles on either side of the main horizontal fault line. Recorded experimental images were centered at the intersection of the primary and secondary planes and encompassed a circular area having a radius of 50 mm.

[16] Figure 3 shows selected frames of the isochromatic fringe patterns recorded for the case of a fault bent −35° toward the extensional side of the specimen. Each frame is identified by the time elapsed following impact and the angle of the bend. These are inscribed on the top left and on the top right corners of the frames, respectively. As in all the experiments conducted in this study, the specimen is loaded at the left edge of the top half. Compressive waves travel

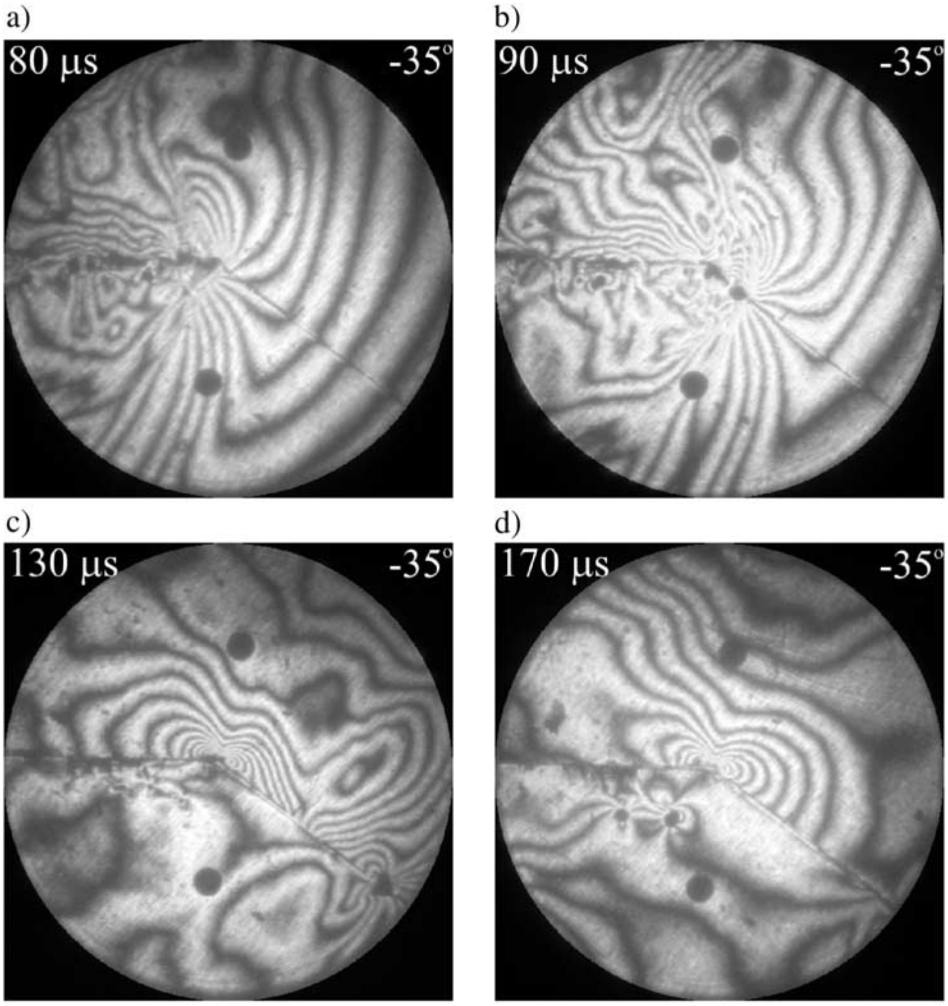

Figure 3. Isochromatic fringe pattern around a mode-II crack propagating at subsonic speed along a weak plane in Homalite-100. The crack continues propagating along a secondary weak path, inclined −35° toward the extensional side of the specimen. Times after impact are (a) 80 μs, (b) 90 μs, (c) 130 μs, and (d) 170 μs. The field of view, of 100 mm, is centered at the intersection of the two weak paths.

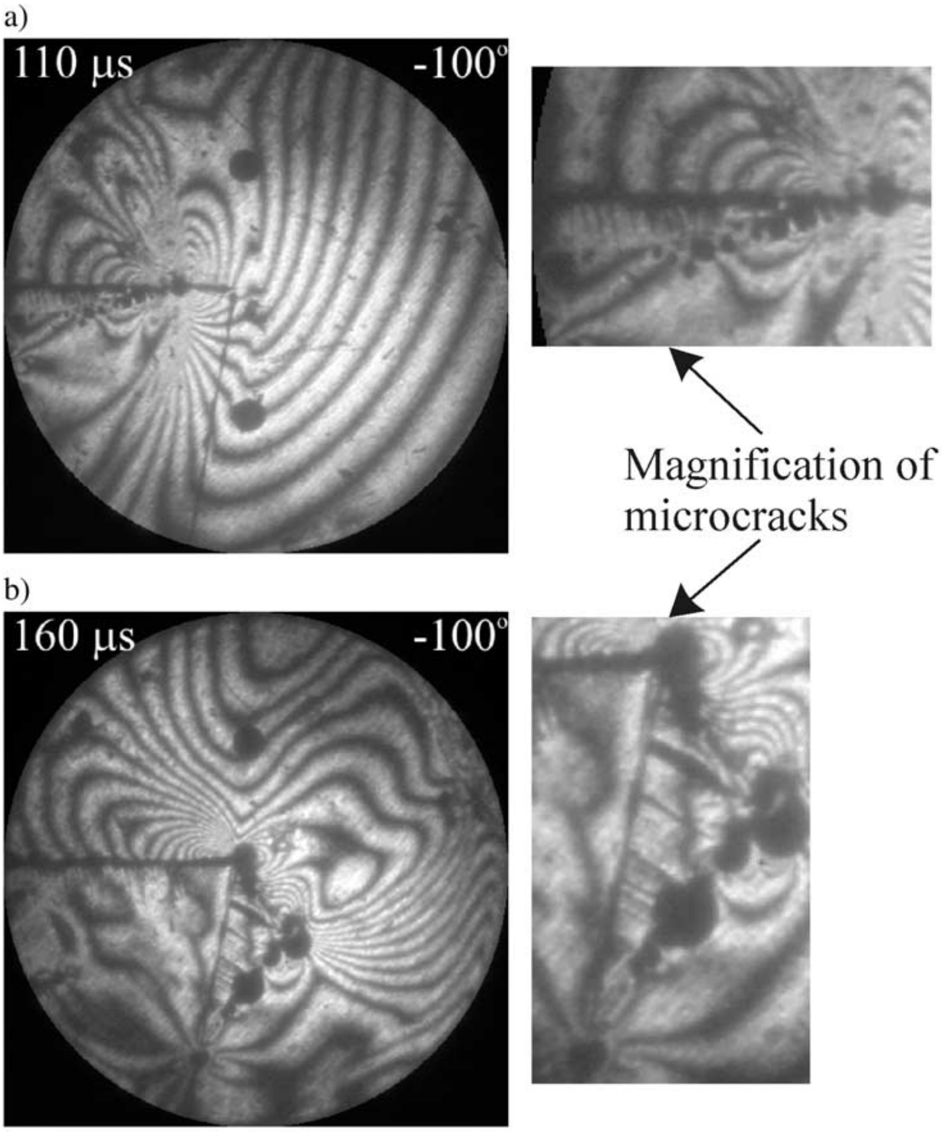

Figure 4. Isochromatic fringe pattern showing a subsonically propagating mode-II crack encountering a weakened plane inclined $-100°$ toward the extensional side of the specimen. Times after impact are (a) 110 μs and (b) 160 μs.

through the specimen predominantly in the top half and are trailed by disturbances corresponding to the shear waves. Finally, the shear crack follows, since its initiation is delayed and it propagates more slowly along the weak plane. Figure 3a shows the crack as it has just reached the intersection of the two paths. The crack tip can be identified using several indicators. First, its location is usually accompanied by a miniscule shadow spot, which is caused by the very high level of deformation within the immediate vicinity of the crack tip. Second, due to high stresses and the presence of discontinuity, the crack tip is always a rallying point for a very large number of fringes. Also present in the frame are fringes, corresponding to the initial stress wave propagation, that are still making their way through the right portion of the field of view as they are preloading the specimen in a combination of shear and compression.

[17] In the next frame, the crack has veered down to follow the bend and in the process has lost some of its energy. Note that this change in direction is also accompanied by a change in stress state. No longer do predominantly mode-II conditions prevail at the crack tip, but rather, the crack assumes a mixed-mode state. This is not apparent from the photograph. However, it will be shown in a later section that this is the case.

[18] At 130 μs, the crack has almost reached the edge of the field of view, with its speed tapered substantially, while still following the weakened interface. Striking in that frame is the fact that the bottom section is almost devoid of fringes and is therefore devoid of stresses. This is caused by the interfacial separation brought about by the moving crack that prevents further transfer of energy between the two sections. The opening component of this decohesion is clear

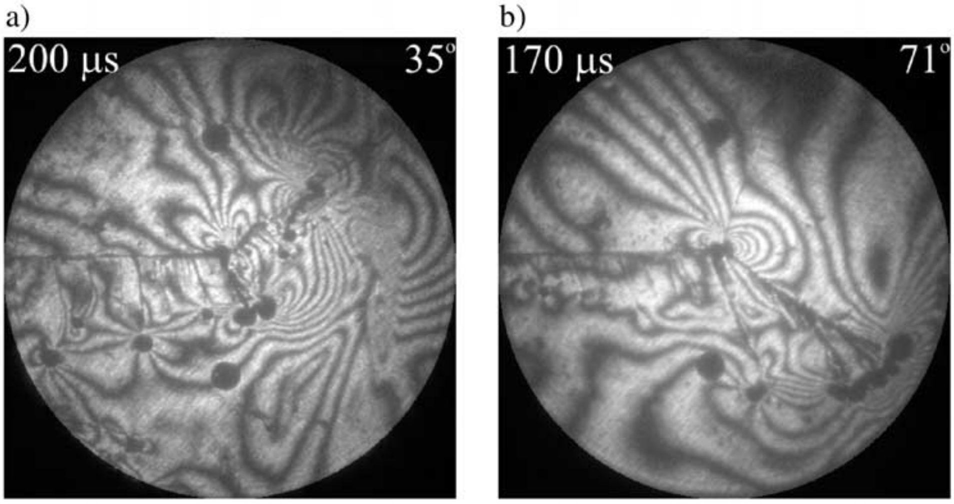

Figure 5. Isochromatic fringe patterns showing subsonically propagating mode-II cracks encountering weakened planes inclined toward the compressional side of the specimens (a) at an angle of 35° and time 200 μs and (b) at an angle of 71° and time 170 μs.

in the next frame, as a narrow white space along the interface testifies to the complete severance between the two sections.

[19] The next two images, presented in Figures 4a and 4b, are of great interest as they depict the behavior of a subsonic crack upon reaching a backward orientated path ($\alpha = -100°$). However, prior to exploring the behavior pertaining to this peculiar geometry, focus will be directed to a character which seems to be universal to all the specimens tested. On the first photograph, a series of shadow spots are present on the extensional side, along the main fault. They correspond to the tips of opening cracks generated as the main shear crack travels along the weak plane. These secondary cracks are periodic and are all inclined at an angle $\alpha^* \sim -79°$ from the direction of crack propagation. The presence of the secondary tensile cracks was explained by *Samudrala et al.* [2002b] by introducing a finite slip-rate-weakening shear cohesive zone behind the shear crack tip. Contact and friction are conjectured to be present along the crack face. Within this model, the biaxial stress state that exists in the cohesive region behind the tip results in maximum principal tensile stresses oriented at an angle $-\alpha^*$ from the interface. This angle is a function of the cohesive strength of the interface, the crack-tip speed, and the level of velocity weakening. Their possible relation to the field observations of periodic tensile microcracking perpendicular to fault planes in rocks has been discussed by *Rosakis* [2002].

[20] The results presented in the next frame (Figure 4b) are not a priori intuitive since they essentially show the crack returning toward the direction from which it originated. The crack has indeed turned the corner and proceeded along the provided $-100°$ path, though at a constantly diminishing speed. Again, secondary tensile, periodic cracks accompany the main crack along the weakened bent path, at an angle of $\alpha^* \sim -71°$. This time, the secondary cracks have grown from the right face of the fault, which has turned extensional with respect to its left side, indicating a change from right-lateral to left-lateral slip as the rupture extends from left to right.

[21] Figure 5a is representative of a specimen having the secondary fault on its compressional side, for a bend angle $\alpha = 35°$. In this frame, the crack has already veered around the corner and is halfway through its progression along the bend, a process accompanied by a slight deceleration. Finally, a case is presented in Figure 5b, for which the moving crack failed to follow the bend but instead penetrated the bulk of the material. In this frame, the secondary weakened path is bent 71° toward the compressional side of the specimen. Here and in all the subsonic cases where the crack failed in its attempt to follow the specimen interface past the bend, the penetration angle into the Homalite was about $-40°$ on the extensional side. Progression into the material is achieved through a dominant mode-I crack, as evident from the symmetric shadow spots surrounding the growing crack tip. This crack propagates steadily at a speed corresponding to 55% of the Rayleigh wave speed, before prevalence of extensive branching in the form of a fan of tensile branches. In addition to this mechanism, failure also proceeds by the prolonged extension of the last of the periodic microcracks (generated just before the bend), which is inclined at $-79°$ to the horizontal.

4. An Energy Approach to Subsonic Crack Deflection

[22] Consider an incipient crack initiating its growth as a result of an applied far-field pure shear loading. The crack will very promptly try to kink or curve relative to its initial direction in an attempt to assume a pure mode-I symmetric state, unless the latter is suppressed by application of suitably oriented compressive stresses or unless the crack is confined to its own plane in a manner similar to that espoused in the current experiments. If the imposed restrictions come to an abrupt end, the crack may breach into the material under mode I, provided the bulk material fracture toughness is low enough relative to the fault plane. If, on the other hand, another weakened path is presented, the crack may elect to follow it, provided motion along that path would generate energy release rate values surpassing

those offered by other alternatives. The said propagation would occur under mixed-mode conditions and is precisely the type of crack extension observed experimentally. It remains to be found whether a study of the energies expanded prior to and potentially after the bend can be used to predict continuation around the bend, and if so, forecast postbend crack speed and mode. A similar methodology was used by *Xu et al.* [2003], who succeeded in predicting the crack speed of a transmitted crack after deflection at a bent. In their case, the approaching crack was purely mode I while the deflected crack propagated under mixed-mode conditions.

[23] Consider a shear crack propagating along a weak bond in an elastic solid. The crack will advance if the material fracture toughness K_{IIc} of the weak bond, lying ahead of it, is attained by the mode-II stress intensity factor K_{II} or if the shear crack growth energy release rate, G_{II}, exceeds the critical shear fracture energy, Γ, associated with K_{IIc}. If however, the crack were to propagate along an infinitesimal kink making an angle θ with the initial crack direction, mixed-mode conditions will in general exist at its tip. Static or dynamic stress intensity factors associated with the infinitesimal kinked crack can both be obtained in terms of the static stress intensity factor, K_{II}, of the prekinked path as follows [e.g., *Broberg*, 1999]:

$$\begin{aligned} K_I^d &= -\frac{3}{4}\left[\sin\left(\frac{\theta}{2}\right) + \sin\left(\frac{3\theta}{2}\right)\right]K_{II}k_I; \\ K_{II}^d &= \frac{1}{4}\left[\cos\left(\frac{\theta}{2}\right) + 3\,\cos\left(\frac{3\theta}{2}\right)\right]K_{II}k_{II}, \end{aligned} \tag{1}$$

where $k_I = [1-(v/c_R)]/\sqrt{1-(v/c_l)}$ and $k_{II} = [1-(v/c_R)]/\sqrt{1-(v/c_s)}$.

[24] Inserted in these two relations are the universal functions of crack-tip speed, k_I and k_{II} [*Freund*, 1990], which account for the kinetic state of the rupture. For the quasi-static case ($v \to 0$) both functions reduce to a value of 1. After crack kinking, equation (1) will be evaluated with $v = v_2$, while prior to kinking, v will be taken to be v_1 and $\theta = 0°$. A dynamic failure criterion based on energy can now be formulated for growth both before and after kinking:

$$G_\theta = \frac{(1-\upsilon^2)}{E}\,\frac{v^2}{(1-\upsilon)c_s^2 D}\left[\alpha_l\left(K_I^d\right)^2 + \alpha_s\left(K_{II}^d\right)^2\right] \geq \Gamma, \tag{2}$$

where

$$D = 4\alpha_l\alpha_s - \left(1-\alpha_s^2\right)^2, \tag{3a}$$

$$\alpha_l = \sqrt{1-\left(v^2/c_l^2\right)}, \tag{3b}$$

and

$$\alpha_s = \sqrt{1-\left(v^2/c_s^2\right)}. \tag{3c}$$

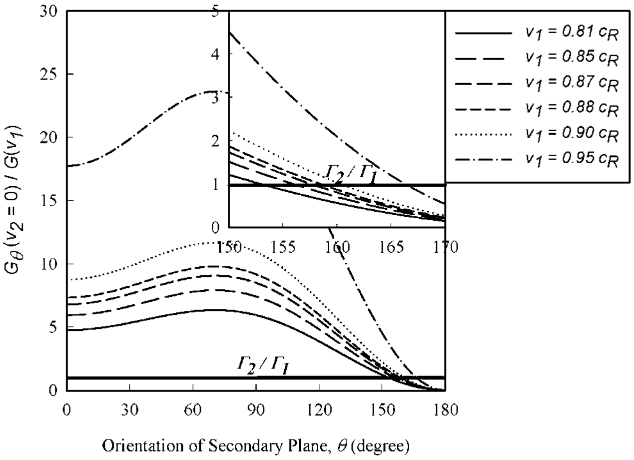

Figure 6. Ratio of the energy release rates of the secondary path to that of the primary path at the limit $v_2 \to 0$. The analysis is valid only for mode-II crack propagating at subsonic speeds along the primary plane. Crack deflection toward the incline is allowed only in the region above the line (Γ_2/Γ_1), which represents the toughness ratio of the incline to that of the main plane.

[25] Inserting equation (1) into equation (2) and taking the ratio of the resulting inequality for values of $\theta = \alpha$ ($v = v_2$) and $\theta = 0°$ ($v = v_1$), respectively, one can conclude that the crack would be able to proceed in the kinked direction only if this ratio reaches or exceeds unity. In the expression to follow, subscript "1" is associated with prebend speed and subscript "2" refers to crack speed after the kink. The requisite inequality, which is valid for both plane stress and plane strain, can be written as

$$\frac{G_{\theta=\alpha,2}}{G_{\theta=0,1}} = \frac{v_2^2 D_1}{v_1^2 D_2} \cdot \frac{9\alpha_{l,2}\left(k_{I,2}\right)^2\left[\sin\left(\frac{\theta}{2}\right) + \sin\left(\frac{3\theta}{2}\right)\right]^2 + \alpha_{s,2}\left(k_{II,2}\right)^2\left[\cos\left(\frac{\theta}{2}\right) + 3\,\cos\left(\frac{3\theta}{2}\right)\right]^2}{16\alpha_{s,1}\left(k_{II,1}\right)^2} \geq 1. \tag{4}$$

[26] Speeds v_2 exceeding zero indicate a propensity for the crack to follow the secondary path, provided the left side of inequality (4) exceeds unity. The expression is plotted in Figure 6 at the limit $v_2 \to 0^+$, for several values of v_1 registered during the experiments. The angles for which the energy ratio is greater than one have therefore the potential for kinked growth. The graphical data of Figure 6 indicate the possibility for crack growth around a bend for all angles inferior to 153°. Note that energy does not differentiate between angular orientation and gives equal probabilistic weight to crack motion along angles θ and $-\theta$. However, the methodology cannot account for the highly compressive state of stress that suppresses the possibility of crack advancement in the major portion of the positive angular domain by producing extensive frictional dissipation associated with crack-face contact. This shortcoming is clearly associated with the assumption that the transmitted crack faces remain traction and dissipation free even for positive kink angles. Consequently, it is felt that this criterion can only be accurate for the extensional side of the specimens. Finally, inequality (4) can also be used as a predictive tool for the speed v_2. By using the equation as an equality, the

speed along the kink can be retrieved, providing motion through the kink angle is allowed as per Figure 6.

5. The Subsonic Singular Crack-Tip Stress Field

[27] The inability of the previous method in segregating positive and negative angles of crack orientation will be remedied by alternatively scrutinizing the dynamic, asymptotic stress fields in the immediate vicinity of a shear crack propagating dynamically in the sub-Rayleigh regime, along a prescribed straight line path representing the "incoming" branch of a kinked weak plane or fault. Let such a crack assume a pure mode-II stress state as it grows along the horizontal direction. Further, let the polar coordinates at the instantaneous crack tip be defined as in Figure 2. The asymptotic form of the stress and deformation fields for such a case has been provided by *Freund* [1990] and is repeated here:

$$\sigma_{11} = -\frac{K_{II}^{d}}{\sqrt{2\pi r}}\frac{2\alpha_s}{D} \cdot \left\{\left(1+2\alpha_l^2-\alpha_s^2\right)\sin\left(\frac{\theta_l}{2}\right)/\sqrt{\gamma_l} - \left(1+\alpha_s^2\right)\sin\left(\frac{\theta_s}{2}\right)/\sqrt{\gamma_s}\right\}, \quad (5)$$

$$\sigma_{22} = \frac{K_{II}^{d}}{\sqrt{2\pi r}}\frac{2\alpha_s\left(1+\alpha_s^2\right)}{D}\left[\sin\left(\frac{\theta_l}{2}\right)/\sqrt{\gamma_l} - \sin\left(\frac{\theta_s}{2}\right)/\sqrt{\gamma_s}\right], \quad (6)$$

$$\sigma_{12} = -\frac{K_{II}^{d}}{\sqrt{2\pi r}}\frac{1}{D} \cdot \left\{4\alpha_l\alpha_s\cos\left(\frac{\theta_l}{2}\right)/\sqrt{\gamma_l} - \left(1+\alpha_s^2\right)^2\cos\left(\frac{\theta_s}{2}\right)/\sqrt{\gamma_s}\right\}. \quad (7)$$

[28] All variables pertaining to these equations have been defined earlier, except for the following:

$$\begin{aligned}\gamma_l &= \sqrt{1-\left(v\sin(\theta)/c_l\right)^2}, \quad \theta_l = \tan^{-1}\left(\alpha_l\tan(\theta)\right);\\ \gamma_s &= \sqrt{1-\left(v\sin(\theta)/c_s\right)^2}, \quad \theta_s = \tan^{-1}\left(\alpha_s\tan(\theta)\right).\end{aligned} \quad (8)$$

[29] These stresses govern deformation only in the immediate vicinity of the crack tip. Further away from the crack tip, geometric and far-field effects can make a significant contribution. These, however, are disregarded, as only the singular stresses are conjectured to contribute to initiation of local bifurcation off the fault path, especially in the absence of static far-field loading as in the experiments described earlier. When substantial levels of far-field loading are present, the above assumption is expected to be less accurate, as rationalized by *Kame et al.* [2003], and in such cases the entire stress state is expected to play an important role. Along every possible kink angle, a combination of the shear stress ($\sigma_{r\theta}$) and the opening hoop stress ($\sigma_{\theta\theta}$) along that direction will act in concert to control the bend direction and overcome local toughness. Thus these stresses, derived from equations (5)–(7), are plotted in Figure 7, normalized with respect to the factor $K_{II}/\sqrt{2\pi r}$, which is common to all stress components. The plots are generated for incoming speeds along the main rupture path at levels of $v_1 = 0.80c_R$ and $v_1 = 0.95c_R$, which encompasses the speed range recorded during the experiments. This approach is indeed the one suggested by *Poliakov et al.* [2002] for the analysis of the more general case of a statically preloaded kinked fault hosting a subsonically growing rupture. As noted by these authors and as is evident from the figure, the dependence of the stresses on incoming speed is striking as can also be surmised from the structure of the above equations. First, within that narrow speed range, the stresses experience an increase in magnitude, with speed sometimes exceeding a factor of two. Second,

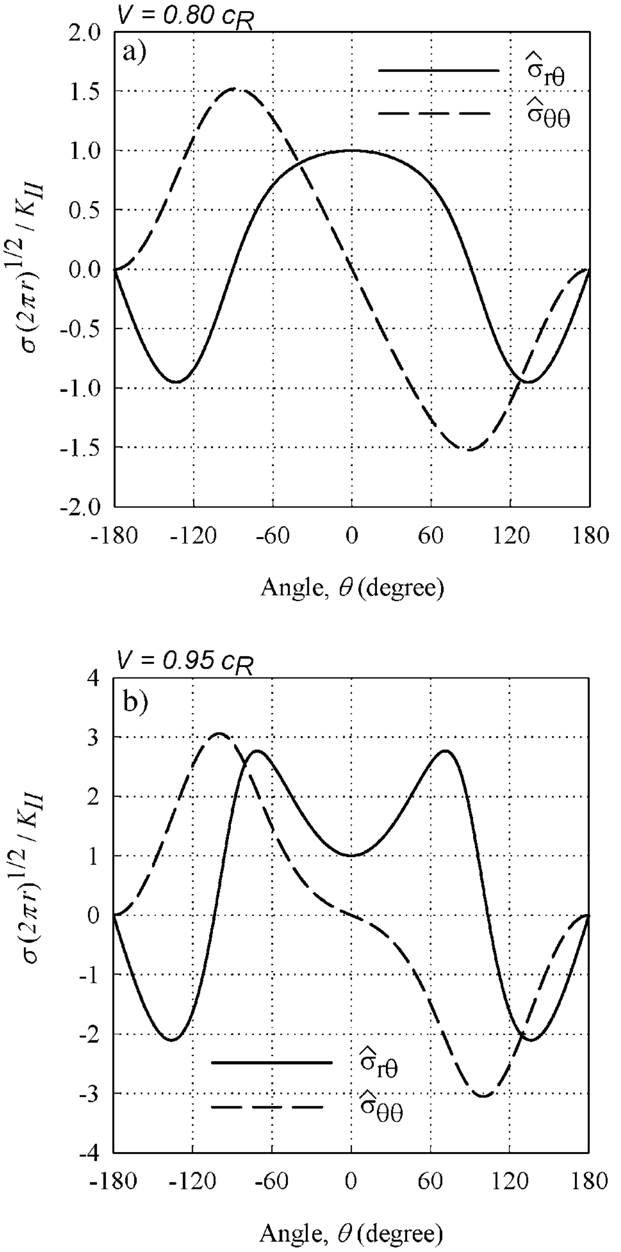

Figure 7. Angular variation of the dynamic crack-tip stress fields for subsonic mode-II rupture occurring at speeds of (a) 0.80 c_R and (b) 0.95 c_R.

for lower speeds, whereas three shear extrema are present at 0° and ±136°, as the incoming speed approaches c_R, the 0° maximum is transposed into two maxima appearing at ±71°. Note also that the shear component is symmetric with respect to the main fault line, whereas the hoop stress is antisymmetric about the same plane. Since the sign of the hoop stresses is positive on the extensional side, the likelihood of activating a branch that lies on that side is far greater than achieving the same on the compressional side, where the hoop stress is negative. This would tend to counteract secondary growth along an upward bend. A criterion based on critical levels of stress can now be formulated.

[30] Generalizing the type of reasoning presented above, one can attempt to formulate a stress-based criterion of kinking that would perhaps describe both opening and shear-dominated crack initiation along a kinked path. For a coherent interface and in the absence of frictional strength, one may follow the work of *Camacho and Ortiz* [1996] and introduce a particular combination of the traction components $\sigma_{\theta\theta}$ and $\sigma_{r\theta}$ acting on the interface, due to an approaching crack tip, as the driving force responsible for decohesion. This driving force should reach or exceed the strength of the interface for cracks to be initiated along it. This criterion is usually stated as follows:

$$\sqrt{\sigma_{\theta\theta}^2 + \beta^2\sigma_{r\theta}^2} \geq \sigma_0, \tag{9}$$

where σ_0 is the opening strength of the interface and β is a weight factor allowing for different levels of opening versus shear strength. In fact, inspection of inequality (9) implies that $\beta = \sigma_0/\tau_0$, where τ_0 is the shear strength of the interface. Relation (9) can now be generalized to include possible contributions to the shear strength of the interface arising from frictional resistance to sliding in the presence of compressive components of traction. A simple way to do so is to require that the generalized traction should reach or exceed a level of strength which also depends on the level of the compressive normal tractions, if present. The kinking criterion will now be expressed as

$$\sqrt{\langle\sigma_{\theta\theta}\rangle^2 + \beta^2\sigma_{r\theta}^2} \geq \beta[\tau_0 + \mu\langle-\sigma_{\theta\theta}\rangle]. \tag{10}$$

[31] In the above inequality, any function enclosed within the bracket is defined as:

$$\langle m\rangle = \begin{cases} 0, & m < 0 \\ m, & m \geq 0 \end{cases}.$$

[32] The combination ($\tau_o + \mu\langle-\sigma_{\theta\theta}\rangle$) represents the shear strength of the interface, augmented by a Coulombic contribution which is activated only if the normal hoop stress is compressive. Indeed, when this normal stress $\sigma_{\theta\theta}$ is compressive, the criterion becomes

$$\sigma_{r\theta} + \mu\sigma_{\theta\theta} = \sigma_{r\theta} - \mu|\sigma_{\theta\theta}| \geq \tau_0, \tag{11}$$

which is exactly the criterion used by *Poliakov et al.* [2002] in their discussion of kinking and branching.

[33] When, on the other hand, $\sigma_{\theta\theta}$ is tensile or zero, then the criterion reduces to the one presented in inequality (9). It should also be noted at this point that the above-postulated criterion has been expressed with respect to the traction components $\sigma_{\theta\theta}(r, \theta)$ and $\sigma_{r\theta}(r, \theta)$ acting on the kinked fault line due to the presence of a dynamically growing crack whose position is at the kink point. The traction components are expressed with respect to distance r measured from the instantaneous location of this crack tip which is moving with speed, v, and can either be sub-Rayleigh or intersonic. In both cases, the general form of the asymptotic stress components is separable in r and θ and can be expressed as

$$\sigma_{r\theta} = \left(A/r^{q(v)}\right)\hat{\sigma}_{r\theta}(\theta, v), \quad \sigma_{\theta\theta} = \left(A/r^{q(v)}\right)\hat{\sigma}_{\theta\theta}(\theta, v). \tag{12}$$

[34] In the above expression, $\hat{\sigma}_{r\theta}(\theta, v)$ and $\hat{\sigma}_{\theta\theta}(\theta, v)$ are the angular distributions of stress and θ is measured counterclockwise from the direction of propagation of the incoming crack. The dependence on the radial distance r is governed by a function of speed $q(v)$ called the singularity exponent, while A is an amplitude factor common to all stress components. In the sub-Rayleigh regime, $A = K_{II}^{d}$, the dynamic mode-II stress intensity factor, and $q(v) = 1/2$ for every v between zero and c_R. For intersonic crack growth, A is denoted by K_{II}^{*d} while $q(v)$ is a continuous and smooth function of crack-tip speed that varies between zero at $v = c_s$ to 1/2 at $v = \sqrt{2}c_s$ down to zero at $v = c_l$. In both speed regimes (with the exception of the exact speed $v = c_s$ and $v = c_l$) the crack-tip field is singular according to the linear elastic model and the stresses become unbounded as $r \to 0$. Indeed, if one substitutes relation (12) into the full-fledged criterion expressed in relation (10), one has

$$\sqrt{\langle\hat{\sigma}_{\theta\theta}\rangle^2 + \beta^2\hat{\sigma}_{r\theta}^2} \geq \beta\left(\tau_o r^{q(v)} + \mu\langle-\hat{\sigma}_{\theta\theta}\rangle\right). \tag{13}$$

[35] As $r \to 0$, the first term of the right-hand side becomes much smaller than all other terms and can be neglected (this is true only for $v \neq c_s$, c_l where $q(c_s) = q(c_l) = 0$). By collecting all contributions in the left-hand side of inequality (13), the criterion can be expressed with respect to a normalized stress, $\hat{\sigma}(\theta, v)$, involving the angular functions of crack-tip speed as follows:

$$\hat{\sigma}(\theta, v) \equiv \left(\sqrt{(\langle\hat{\sigma}_{\theta\theta}\rangle/\beta)^2 + \hat{\sigma}_{r\theta}^2} - \mu\langle-\hat{\sigma}_{\theta\theta}\rangle\right) \geq 0. \tag{14}$$

[36] The expression no longer involves the shear bond strength τ_0. Inequality (14) suggests that to first order and in the absence of substantial static far-field stress, the approaching crack tip has to overcome only the frictional strength $\mu\langle-\hat{\sigma}_{\theta\theta}\rangle$ caused by its own asymptotic and singular field through compression and the resulting frictional resistance. This analysis is valid only for a strictly asymptotic interpretation of the rupture behavior. If, on the other hand, a cohesive model were to be implemented, neglecting the fault strength would be inappropriate, and the argument would be subject to modification. The variable $\beta \equiv \sigma_0/\tau_0$ was determined experimentally to be 1.875. The friction coefficient μ in this crude model should be identified as the dynamic friction coefficient and lies much

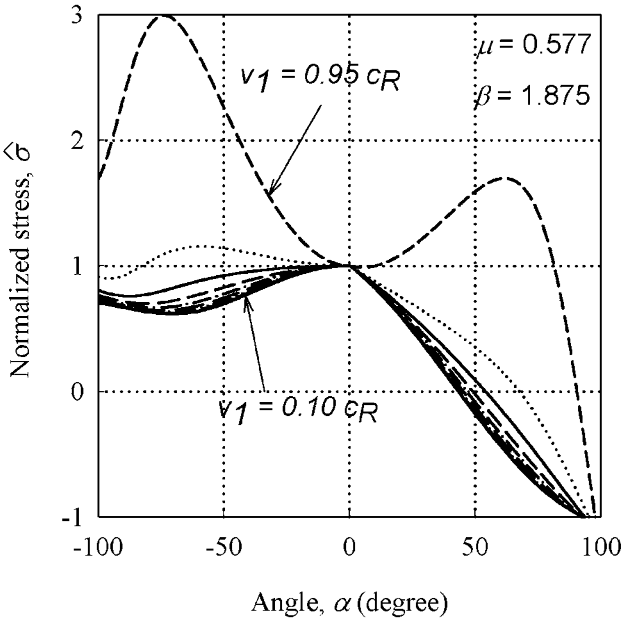

Figure 8. Variation of the normalized driving stress measure $\hat{\sigma}(\theta, v)$ as a function of incoming rupture speed, v_1.

below the static value measured to be 0.84. In the first series of discussions, μ will be set to tan (30°) or 0.577. This is a value very close to the one assumed by *Harris et al.* [2002] in their recent study of intraearthquake triggering in relation to the 1999 Izmit earthquake. A parametric investigation that follows the initial analysis will allow μ to drop all the way down to 0.1.

[37] The dependence of the stresses on the speed of the incoming crack again becomes obvious upon inspection of the angular variation of the stresses plotted in Figure 7, as is the speed dependence of $\hat{\sigma}(\theta, v)$ plotted in Figure 8. Note, in particular, that as the incoming crack speed approaches c_R, the angular stress variation deviates substantially from those corresponding to lower values of velocities, all of which congregate within a relatively limited range. This is expected, as Figures 6 and 7 do forecast a unique separation near c_R.

[38] Finally, it should be noted that, given a fixed speed, v_1, of the incoming crack, for those kink angles $\alpha < 0$ such that $\hat{\sigma}(\alpha, v = v_1) < 0$, the criterion would preclude any crack growth along the weak kinked path. On the other hand, for angles such that $\hat{\sigma}(\alpha, v_1) \geq 0$, crack growth along a kink would be favored. For the latter case, the kinked crack would propagate with a speed $v_2 \neq v_1$. The magnitude of $\hat{\sigma}(\alpha, v_1)$ represents the level of crack driving force available to an outgoing kinked crack at each angle α due to the arrival of an incoming crack whose speed was v_1. One would expect the speed of the outgoing crack to vary proportionally to this level of driving force. This suggestion will be investigated experimentally in the following sections.

6. Discussion of the Subsonic Results

[39] In this section, the experimental, results will be revisited and compared to the two criteria developed in the previous sections. Raw speeds were first obtained by recording the location of the crack tip from the high-speed camera records and by using a central difference scheme to differentiate the crack length time history. These speeds were then normalized by c_R and plotted for each experiment, with respect to instantaneous crack-tip location. Figure 9 shows such a speed history for the case of a secondary path bent 35° toward the compressional side of the specimen. The dashed vertical line dividing the plot, with an abscissa value of zero, represents the intersection point between the main horizontal and the incline planes. In other words, it marks the location of the kink. Therefore data points left of the vertical line refer to progression along the main path, and to the right of the vertical line are data points corresponding to motion along the incline. The crack cruises along the primary fault within a narrow range, arriving at the corner of the bend with a speed of $v_1 = 0.88c_R$. Following kinking around the bend, a drop in speed to $v_2 = 0.82c_R$ is recorded. Only very few data points are available along the secondary path. These, however, do not show much variation, which would indicate that a steady state speed is reached rather quickly in this case. Figure 10 includes several plots of the same general geometry corresponding to secondary faults situated on the extensional side of the specimen. In the first plot (Figure 10a), measured speeds at kink angles of $-35°$ and $-71°$ are combined. Kink angles of $-100°$ and $-103.5°$ are combined in Figure 10b. Common to these four cases is the decrease in crack-tip speed following the intersection of the two paths. This speed drop becomes more pronounced as the angles become more obtuse. Also, the general trend is for the speed along the secondary fault to diminish further before attaining a steady state level.

[40] Some level of uniformity in the interpretation of these results is accomplished by computing the ratio of

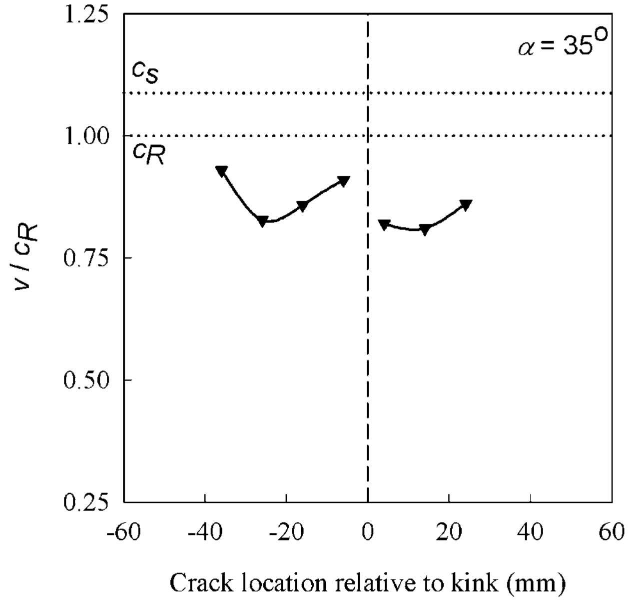

Figure 9. Speed history for a crack propagating in mode II along a weak plane, in the subsonic regime, and encountering an incline at 35° toward the compressional side of the specimen.

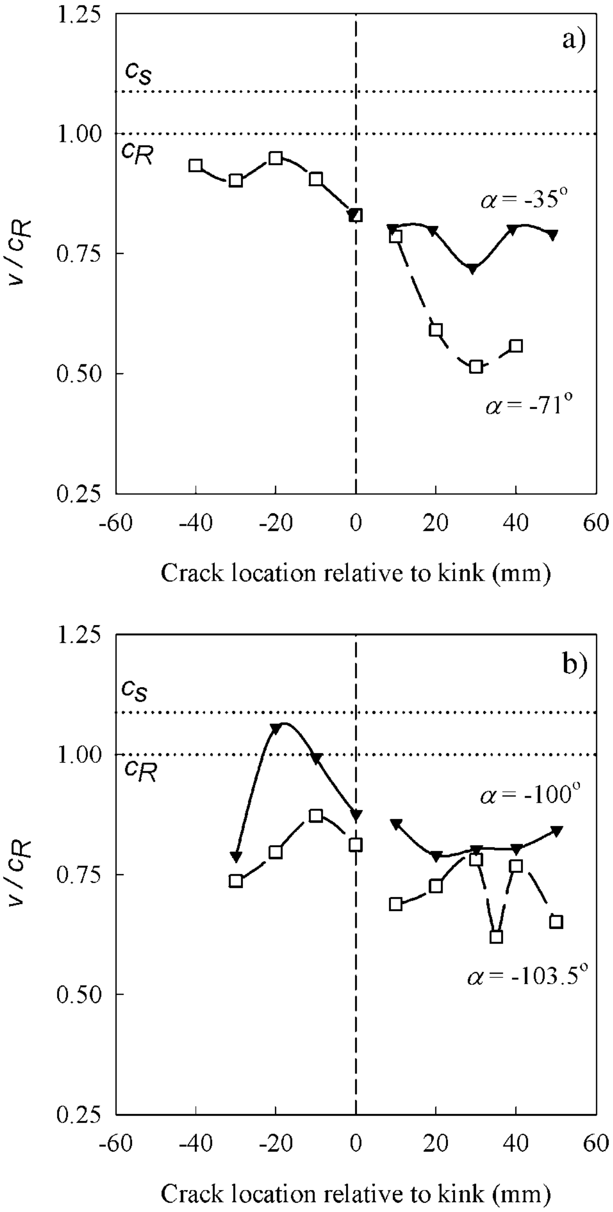

Figure 10. Speed history for a crack propagating in mode II along a weak plane, in the subsonic regime, and encountering a secondary weak plane. All fault bends are toward the extensional side of the specimens at angles of (a) −35° and −71° and (b) −100° and −103.5°.

the initial speed of the moving crack recorded just after kinking to the crack speed along the primary plane just before kinking for the various specimens tested. The speed ratio was then plotted with respect to the kink angle of the secondary fault, as presented in Figure 11. The reference point is at an angle of 0°, at the vertical line separating the positive and negative portions of the abscissa, for which case, $v_2/v_1 = 1$. On the extensional side, there is a gradual decrease in the speed ratio with increasing angle, up to −100°, after which point the drop in speed ratio becomes drastic. At −136° and beyond, the crack can no longer continue on the secondary path, but instead branches into the bulk material. At an angle of 35°, the initial branching crack speed is slightly lower than that of its tensile counterpart. Finally, at 71° and beyond, further crack extension is not possible. Note that no data were available between −103.5° and −136° or between 35° and 71°. Thus the exact angles for which secondary fault triggering is unattainable is not known.

[41] The experimental results are highly dependent upon the incoming crack-tip speed, confirming the original observation of *Poliakov et al.* [2002]. Because v_1 varies between experiments, the results are better understood if experiments and theoretical projections (left-hand side of inequality (4)), which includes the same speed dependence, are viewed simultaneously. The theoretical predictions based on the energetic arguments are superimposed on the plot for the extensional side. Only the discrete theoretical points are computed by using, in each case, the exact incoming crack speed measured in each individual experiment. There is excellent agreement between the two from 0° to −100°, where theoretical and experimental data partially conceal each other. At −136°, the theory predicts a sharp drop in v_2, not drastic enough, however, as to suppress secondary branching, as observed experimentally. Recall that Figure 6 would forecast crack arrest at the end of the primary plane only for secondary plane angles more obtuse than $\alpha = -153°$. Nevertheless, this difference constitutes but a mere shift in the data, whereas overall behavior and trends remain identical. Thus it can be concluded that the energy criterion may be used with great confidence in studying extensional fault branching.

[42] Next, the focus must be placed on the theoretical considerations based on the singular crack-tip stress field and the stress criterion of inequality (14). To that aim, the experimental data are plotted again in Figure 12, accompanied by visual representation of inequality (14) at locations corresponding to the experiments. Theoretical points are normalized to unity for the case of a straight, unkinked fault ($\alpha = 0°$). It is suspected here that there exists a correlation between predicted driving stress and normalized kink speed. Consequently, the two normalized quantities are plotted on

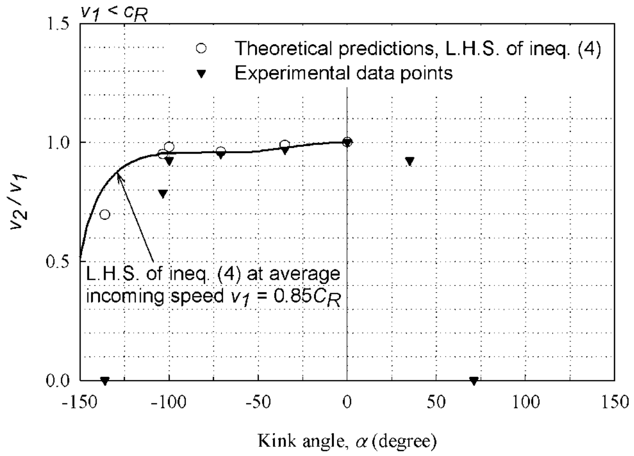

Figure 11. Experimentally measured and theoretically predicted ratio of outgoing to incoming crack speeds as the cracks are engaged along fault bends of various inclinations. Theoretical predictions v_2/v_1 are based on the energy criterion. Incoming mode-II cracks are subsonic.

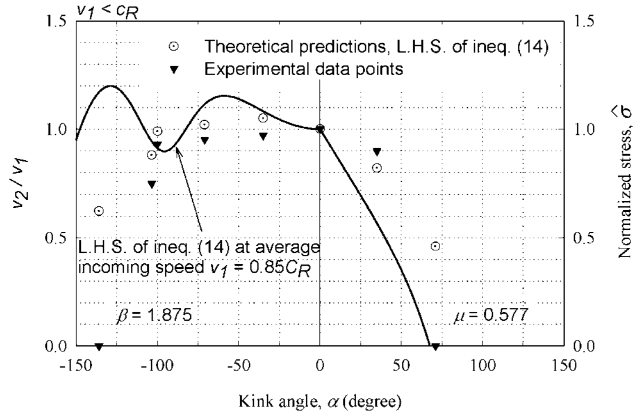

Figure 12. Experimentally measured and theoretically predicted ratio of outgoing to incoming crack speeds as the cracks are engaged along fault bends of various inclinations. Theoretical predictions of the normalized driving stress measure $\hat{\sigma}(\theta, v_1)$ are based on the asymptotic crack-tip stress field. Incoming mode-II cracks are subsonic.

the same graph to verify this suspicion. The first few theoretical points, up to $-100°$, overestimate the experimental ones only by a small percentage. The speed ratios at $-103.5°$ are not as accurate but still well predicted by the theory. At $-136°$, on the other hand, the theory highly overestimates the speed ratio. Based on the crack-tip stress field, branching would also be expected in the remaining angles corresponding to the extensional side of the fault, though with a greatly reduced probability. On the compressional side, the normalized branching speed is overestimated at 71° but differs only slightly at 35°. Though not fitting impeccably for each angle studied, the relative normalized driving stress levels from inequality (14) offer the same overall trends as do speeds obtained experimentally. The predictive abilities of inequality (14) are comparable to those of inequality (4). Furthermore, the former presents the additional benefit of predicting the level of propagation possible along a kink situated on the compressional side. Predictions of inequality (14) over the pertinent range of data, for a single average speed v_1, are also presented in Figure 12. Overall agreement with the experimental data is present. However, the plot is burdened by oscillations that make it depart from full accord with the experimental data. It must be reemphasized, however, that the experimental data correspond to different values of incoming crack-tip speed, while the continuous $\hat{\sigma}(\theta, v)$ curve was calculated assuming a constant incoming speed value taken to be the average of the experimentally measured incoming crack-tip speeds. Therefore this apparent dissension does not detract from the excellent predictive capabilities of the crack-tip stress field approach, which is very apparent in the comparison between discrete solid or open symbols.

7. Experimental Observations in the Intersonic Regime

[43] The remainder of this paper is devoted to examining the behavior of incoming intersonic cracks as they reach the alternate kinked path. In the intersonic regime, crack initiation is followed by sudden acceleration to levels below c_l, and finally by deceleration to steady state values near $\sqrt{2}c_s$. It must be noted that the recent work by *Samudrala et al.* [2002a] has identified the region between c_s and a characteristic rupture speed close to but higher than $\sqrt{2}c_s$ as being unstable. Speeds between $\sqrt{2}c_s$ and c_l were identified as stable. The exact value of this characteristic speed, delineating the border between the stable and the unstable regimes, was found to depend on the nature of the bond strength and on other parameters of the slip-weakening cohesive model used in their analytical study. The minimum value of this characteristic speed corresponds to high bond strength and is equal to $\sqrt{2}c_s$. This observation is consistent with the early stability results obtained by the slip-weakening models of *Burridge et al.* [1979] and later obtained numerically by *Needleman* [1999] and *Abraham and Gao* [2000] on the basis of cohesive element and atomistic calculations, respectively. It is also noteworthy that at an entirely different length scale, *Bouchon et al.* [2001] reported stable intersonic rupture speeds slightly higher than $\sqrt{2}c_s$ occurring over the segment of the North Anatolian fault, east of the hypocenter of the 1999 Izmit earthquake.

[44] Figure 13 illustrates several cases for which crack propagation along the primary plane reached steady state intersonic speed prior to arriving at the intersection with the secondary plane. An important feature identifying the intersonic nature of the crack propagation is revealed in Figure 13a. In that frame, the presence of a shear stress Mach cone is clear. It is characterized by a wedge-shape structure, separated from the remainder of the fringes by a line of discontinuity along which there is a jump in stresses. The extremity of the Mach cone coincides with the instantaneous location of the crack tip. As an alternative to differentiating consecutive crack-tip locations with respect to time, the crack speed, v, can also be obtained from the Mach angle, $\psi = \sin^{-1}(c_s/v)$. Because of its superior accuracy, evaluation of crack-tip speed by means of measuring the inclination of the Mach cone is used whenever available.

[45] A sequence showing progression of the crack as it approaches and follows a secondary plane bent at an angle $\alpha = -35°$ is presented in Figures 13a and 13b. As the crack turns onto the bend, its state of the motion is no longer one of primary shear, as a normal component is now associated with it. Figure 13b shows the crack as it nears the edge of the field of view, along the secondary plane. The presence of the Mach cone clearly indicates that the crack has retained its intersonic nature beyond the bend.

[46] Next is a frame from a specimen with its secondary plane bent at angle of $-56°$ (Figure 13c), recorded after kinking. Along the secondary plane, the contrast between the behavior of this specimen and the previous one is striking. First, the Mach structure is no longer present, an indication of a sharp drop in speed of the crack from its prekinked, intersonic state. Instead, vague remnants of the Mach cone still drift on the top and bottom sections and are fully dissociated from the crack tip, which is visible on the secondary plane. Upon reaching the kink site, the tip of the cone detaches itself from either of the two paths, and in the process, becomes blunt. The entire structure eventually

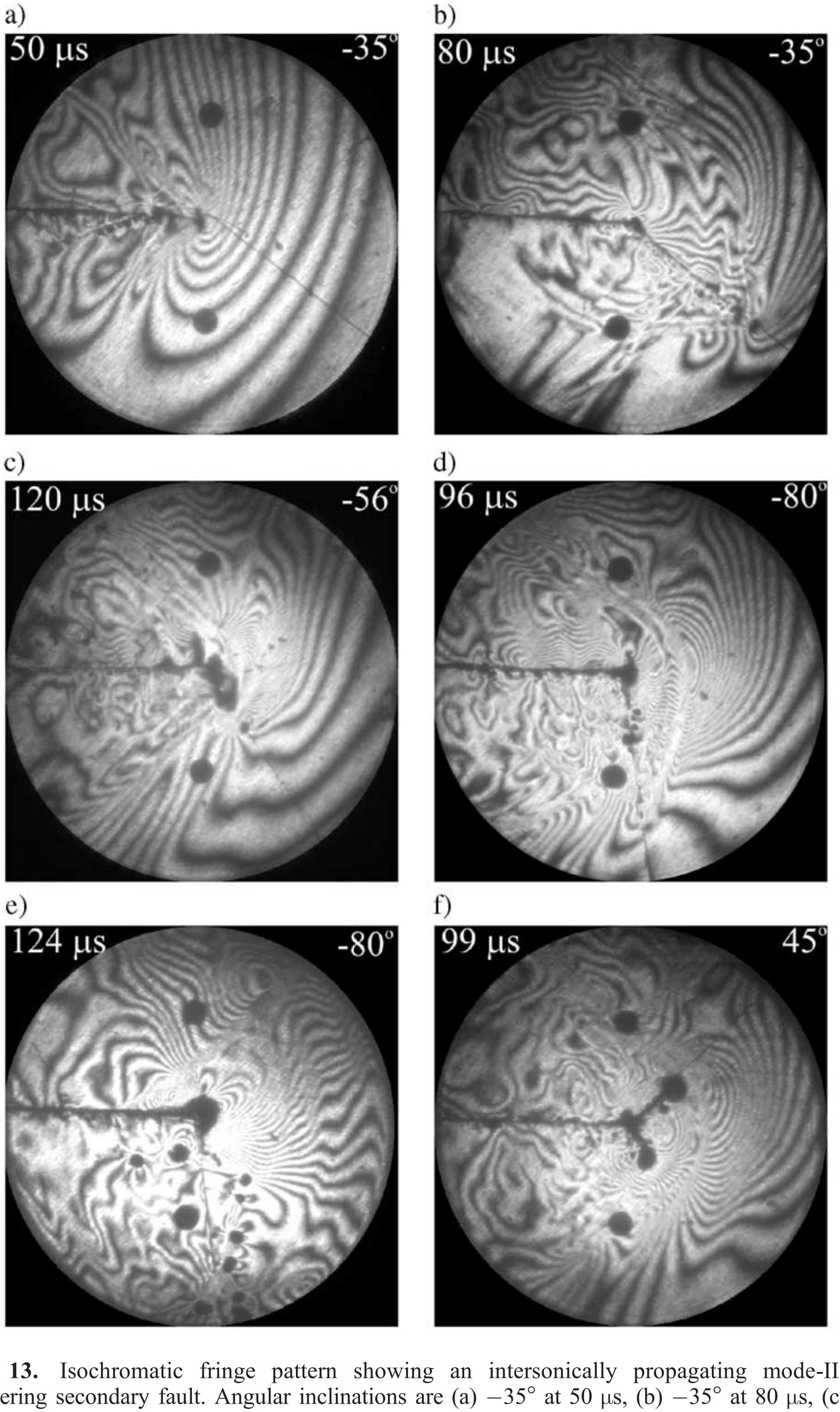

Figure 13. Isochromatic fringe pattern showing an intersonically propagating mode-II crack encountering secondary fault. Angular inclinations are (a) −35° at 50 μs, (b) −35° at 80 μs, (c) −56° at 120 μs, (d) −80° at 96 μs, (e) −80° and 124 μs, and (f) 45° at 99 μs after impact. The fault bends it toward the extensional side in the first five frames and toward the compressional side in the last frame.

acquires a semihemispherical shape before finally disappearing. In addition to the crack speeds along the incline path having fallen to within the subsonic range, it is noted that microcracks are absent from the secondary plane, whereas they were still prominent on the primary plane. Postmortem examination of four specimens confirms that the kinked portion of the interface does not feature any microcracks. Thus it may be concluded that crack-tip stress states have rotated in such a manner as to align the principal tensile stresses perpendicularly to the kinked interface, opening a path to the crack in primarily mode I, thereby minimizing any mode-II component. A primarily tensile stress state would minimize crack-face contact as well as any mode-II components, conditions necessary for the formation of secondary tensile microcracks.

[47] The sequence presented in Figure 13d displays yet another trend. The figure shows a specimen having its secondary path rotated −80° toward the extensional side. The frame shows the crack after it has traveled two thirds of the way along the incline. Some similarity exists with the previous case having the weakened kinked path at $\alpha = -56°$. Indeed, upon reaching the kink, the Mach cone overshoots past the intersection of the two paths, and its acute angle becomes blunt. However, unlike the previous case, the bottom edge of the discontinuous envelope remains attached to the moving crack, whereas the edge situated above the primary plane has barely shifted. This results in a very pronounced asymmetry of what was formerly the Mach cone enclosure. Following the progress between several frames, the apparent behavior is that of an extremely blunted and obtuse angle being rotated counterclockwise about a fixed point along the extended primary plane, such as to allow the bottom section to retain its association to the crack tip. Nevertheless, crack propagation along the incline does resume its advance in the intersonic regime. Though not very distinct, a new Mach cone has regenerated, moving downward along the secondary plane. The narrow inclination of the secondary shock wave confirms the large acceleration experienced by the propagating crack along that path.

[48] In Figure 13e, secondary tensile cracks developing from the alternate weakened path are also noticeable. The photograph is specifically meant to put these microcracks in evidence, the frame having been recorded after full propagation of the main crack. The location of these tensile cracks is indicated by the large shadow spots present at their tips. Most important here is that they are located to the right rather than to the left of the incline, indicating an abrupt shift from right- to left-lateral slip after the fault kink. This establishes a change in the sign of shear after kinking.

[49] The last photoelastic fringe pattern (Figure 13f) represents a marked departure from all the previous intersonic cases, as the angle of the secondary path is relatively large (45°) and is situated on the compressional side. Narrower compressional kink angles were surmounted by the cracks almost as effortlessly as their extensional counterparts. In the present frame, the crack is only a few millimeters past the intersection of the two paths and progresses slowly and laboriously within the subsonic regime. Concurrently, a branch is initiated into the bulk of the material, at an angle of −60° on the extensional side, and extends at approximately half the speed of the secondary kinked crack or 55% of the Rayleigh wave speed. It will be shown later that −60° is a principal stress direction. Thus for the present configuration, despite the higher toughness of the bulk material, the crack finds it as equally effortless to branch into the bulk material in mode I as it is to follow the incline, weakened path. Further increasing the angle that the alternate path makes with the primary plane prohibits entry onto the incline, leaving only a slow-moving mode-I crack to proceed into the bulk material, away from the incline. Also, note that for slightly lower secondary plane inclination ($\alpha = 42°$) in which a dual path is still present, entry into the homalite occurs less forcefully, with a speed of $0.25c_R$, while the concurrent continuing compression/shear crack propagation along the secondary plane remains intersonic.

8. The Intersonic Singular Crack-Tip Stress Field

[50] Consider a crack extending in its own plane under pure shear in a homogeneous, isotropic material. The speed at which the crack is moving need not be constant as long as it is continuous and varies smoothly. As in the previous sections, let there be a moving Cartesian coordinate (η_1, η_2) attached to the crack tip, with related polar coordinates (r, θ), as shown in Figure 2. Then the near-tip singular stress field has been determined by *Freund* [1979] and is expressed as

$$\sigma_{11} = \frac{K_{II}^{*d}}{2\alpha_l\sqrt{2\pi}}\left[\frac{-\left(1+2\alpha_l^2+\hat{\alpha}_s^2\right)}{r_l^q}\sin(q\theta_l) + \frac{\left(1-\hat{\alpha}_s^2\right)\sin[\mathrm{sgn}(\eta_2)q\pi]}{\left(-\eta_1-\hat{\alpha}_s|\eta_2|\right)^q}H(-\eta_1-\hat{\alpha}_s|\eta_2|)\right], \tag{15}$$

$$\sigma_{22} = \frac{K_{II}^{*d}}{2\alpha_l\sqrt{2\pi}}\left[\frac{\left(1-\hat{\alpha}_s^2\right)}{r_l^q}\sin(q\theta_l) - \frac{\left(1-\hat{\alpha}_s^2\right)\sin[\mathrm{sgn}(\eta_2)q\pi]}{\left(-\eta_1-\hat{\alpha}_s|\eta_2|\right)^q}H(-\eta_1-\hat{\alpha}_s|\eta_2|)\right], \tag{16}$$

$$\sigma_{12} = \frac{K_{II}^{*d}}{\sqrt{2\pi}}\left[\frac{1}{r_l^q}\cos(q\theta_l) - \frac{\cos[\mathrm{sgn}(\eta_2)q\pi]}{\left(-\eta_1-\hat{\alpha}_s|\eta_2|\right)^q}H(-\eta_1-\hat{\alpha}_s|\eta_2|)\right], \tag{17}$$

where

$$r_l = \sqrt{\eta_1^2+\alpha_l^2\eta_2^2}, \qquad \theta_l = \tan^{-1}(\alpha_l\eta_2/\eta_1),$$
$$\hat{\alpha}_s = \sqrt{\left(v^2/c_s^2\right)-1}, \qquad q = (1/\pi)\tan^{-1}\left[4\alpha_l\hat{\alpha}_s/\left(1-\hat{\alpha}_s^2\right)^2\right]. \tag{18}$$

Functions "sgn" and "*H*" are the sign and the Heaviside functions, respectively. Equations (15)–(17) are valid only if the crack-tip-dominant singular terms are more significant than the remainder of the expansion.

[51] The Heaviside step function indicates a discontinuity in the stresses that translates into the formation of the two edges of the Mach cone. This solution to the intersonic problem features another major difference from the subsonic case in that singularity exists not only at the crack tip but also along the Mach front and governs the intensity of the stress jump across the Mach cone. In addition, when v is precisely equal to $\sqrt{2}c_s$, the step functions vanish, thereby pointing to the disappearance of the Mach cone at that peculiar speed and to the return of singularity solely to the crack tip. Special conditions resulting in the disappearance

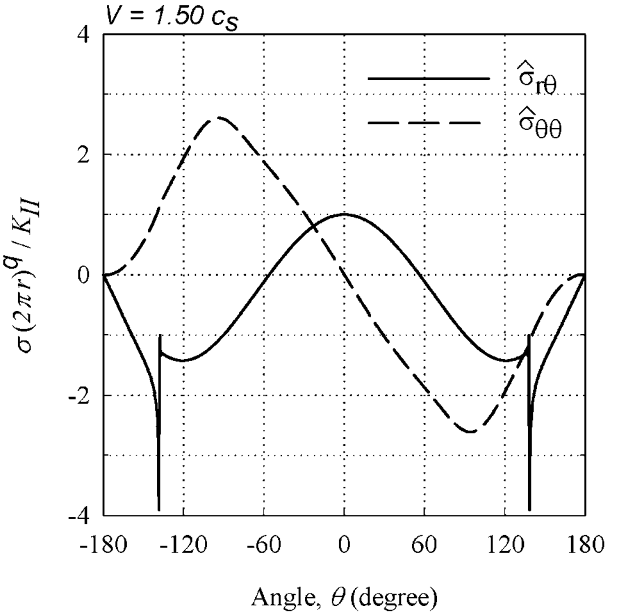

Figure 14. Dynamic crack-tip stress fields for intersonic mode-II rupture occurring at a speed of 1.50 c_s. The normalized stresses are plotted with respect to angular inclination.

of the Mach wave are often referred to as radiation free [*Gao et al.*, 1999]. Finally, for intersonic cracks, the strength of the singularity is 1/2, as in the subsonic case, only for $v = \sqrt{2}c_s$. On either side of that special speed, q monotonically decreases to be zero at $v = c_s$ and $v = c_l$.

[52] To further understand the behavior of a mode-II crack extending intersonically, polar component of stresses are obtained from equations (15) to (17) and plotted in Figure 14 for $v = 1.5\ c_s$. This particular speed of 1.5 c_s is chosen based on experimental evidence that in most cases the running crack hovers slightly above $\sqrt{2}c_s$ while following a straight path. Also recall theoretical predictions that the segment between $\sqrt{2}c_s$ and 1.5 c_s requires the minimum amount of critical load to sustain intersonic crack propagation and is therefore an obvious region for the crack speed to try and achieve steady state. The relevant stresses, $\sigma_{\theta\theta}$, $\sigma_{r\theta}$, are normalized through multiplication by (r_l^q/K_{II}^{*d}) The resulting angular variations $\hat{\sigma}_{\theta\theta}$ and $\hat{\sigma}_{r\theta}$ are plotted as a function of angular location, in the immediate vicinity of the crack tip. Radial stresses act in the direction of crack growth and are therefore not pertinent to the current problem.

[53] Since the crack is advancing due to shear loading, the effect of $\sigma_{r\theta}$ will be prevalent. The main features of this stress component are reviewed. As expected, the maximum shear occurs at $\theta = 0°$, along the plane of the crack, and is symmetric about that plane. On either side of the crack plane, the shear stress decreases to zero at $\theta \sim \pm 56°$. This angle is therefore a principal stress direction. Thereafter, the sign of shear changes to attain an extrema at ±121° before returning to zero at ±180°. This latter portion of the curve is punctuated by a strong discontinuity at ±138°, which again corresponds to the Mach cone. The location of this discontinuity gradually shifts toward larger angles with increasing crack speed and toward smaller angles as speed decreases. The exact position is given by $\theta = (\pi - \sin^{-1}[c_s/v])$.

[54] The opening stress $\sigma_{\theta\theta}$ is asymmetric with respect to the crack plane and is zero directly ahead of the crack. Therefore the solution correctly recognizes the existence of a pure shear condition at that location. The profile of the hoop stress as it varies with orientation is akin to that of an inverted sine function, with its extrema shifted to ±94°.

[55] From the above, the shear stress distribution offers equal probability for kinking toward either side of the primary crack plane. On the other hand, the sign of the hoop stress clearly supports growth toward the extensional side. A criterion for determining whether a propagating crack can leap from the main path onto an incline can be appropriated from the subsonic case. Inequality (10), which was used with much success in the subsonic regime, will again be adopted here to establish the likelihood of decohesion of the weak bond along an incline as it is being approached by an intersonic crack along the primary plane. In the present case, normalization of relation (10) will be implemented with respect to (K_{II}^{*d}/r_l^q) and conditions as $r_l \rightarrow 0$ will be considered. This results in inequality (14) involve only the angular variations $\hat{\sigma}_{\theta\theta}$ and $\hat{\sigma}_{r\theta}$, which are also strong functions of rupture speed.

9. Discussion of the Intersonic Results

[56] In this section, the experimental results will be reviewed in the light of the aforementioned analytical solution. First, speed histories of the moving cracks within the field of view are presented. Figure 15a shows crack speeds of two specimens having weakened secondary planes inclined at an angle $\alpha = -10°$ on the extensional side. Speeds are normalized with respect to c_s. Most of the speeds recorded are based on the Mach cone angle. At locations where this information was ambiguous or unavailable, speeds were based on a three-point regression of the crack length history. The figure shows the prekink speed to be mostly confined to the range between $\sqrt{2}c_s$ and c_l. The crack speed retains its prekink value over the entire length of the incline.

[57] The next set of experiments, for $\alpha = -35°$, shows a slight decline in speed right after the crack engages along the secondary plane (Figure 15b). Again, in this case the crack speed along the incline remains nearly constant near its initial level. At $\alpha = -42°$ (Figure 15c), the initial postkink speed suffers slight postkink speed deterioration when compared to shallower angles. Once more, in this case, the speed remains fairly constant along the incline. The same figure includes data for $\alpha = -53°$ and features an initial postkink decrease in speed followed by a slight increase and a plateau. Very drastic is the loss of speed suffered by the crack as it veers toward a secondary plane bent at −56°. Indeed, for both tests presented (Figure 15d), the crack speed has fallen either to c_s or to within the subsonic range in a very short time but then recovers its speed back into the intersonic range and oscillates. A lesser drop in speed is observed for $\alpha = -60°$ (Figure 15e). However, very large speed variations follow as the crack speed continues its decline to below c_R. Figure 15f reveals the beginning of a transition. For secondary path inclinations $\alpha = -65°$ and $\alpha = -75.5°$, the postkink crack speed remains constant and increases, respectively, compared to its individual prekink levels. The next two angles ($\alpha = -80°$ and −90°) capture further drastic gains in speed following

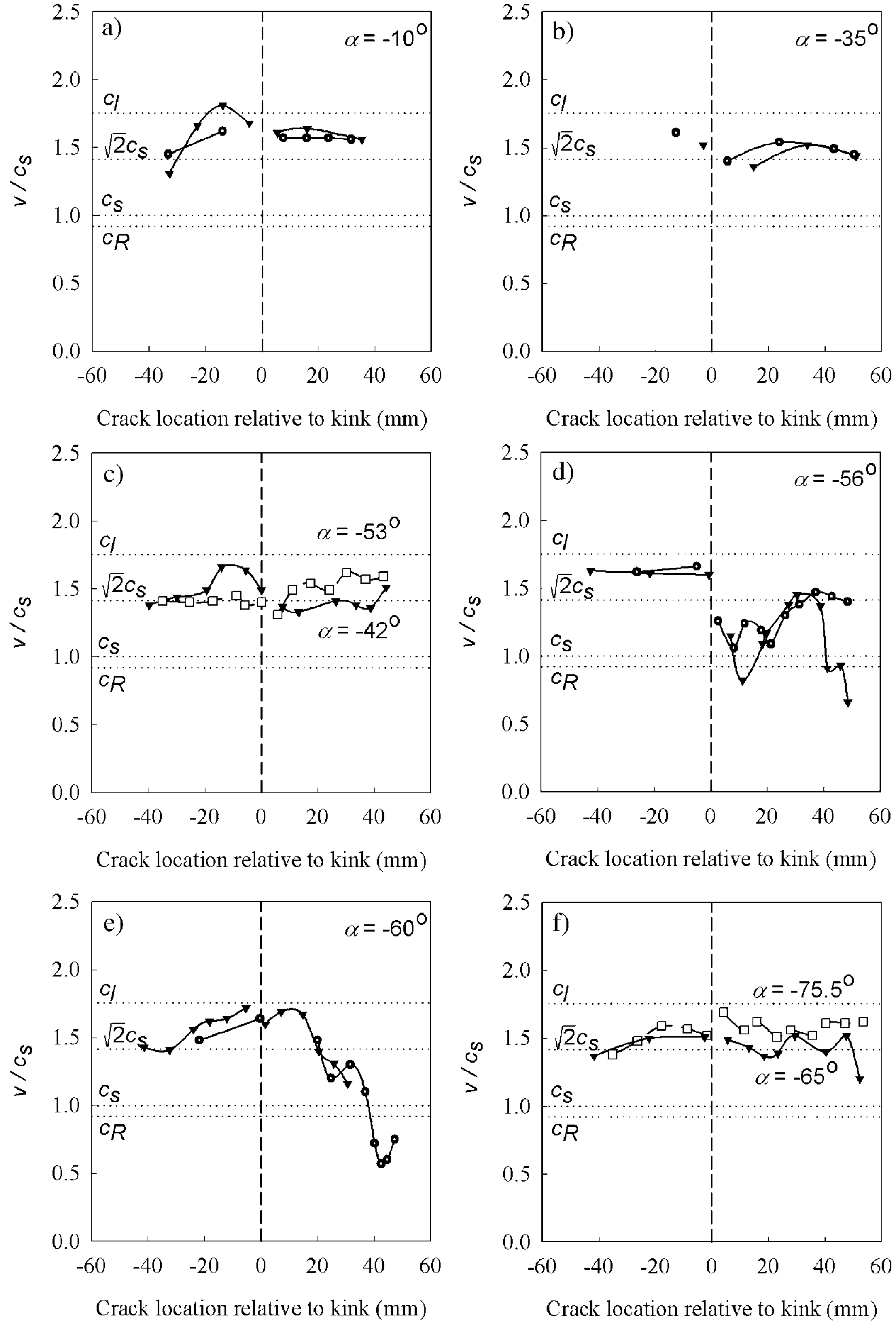

Figure 15. Speed history for a crack propagating in mode II along a weak plane, in the intersonic regime, and encountering a secondary fault path. The following inclines are toward the extensional side of the specimens: (a) −10°, (b) −35°, (c) −42° and −53°, (d) −56°, (e) −60°, (f) −65° and −75.5°, (g) −80°, (h) −90°, and (i) −100°. Inclines oriented toward the compressional side of the specimens are (j) 10° and 35°, (k) 42° and 45°, and (l) 53°.

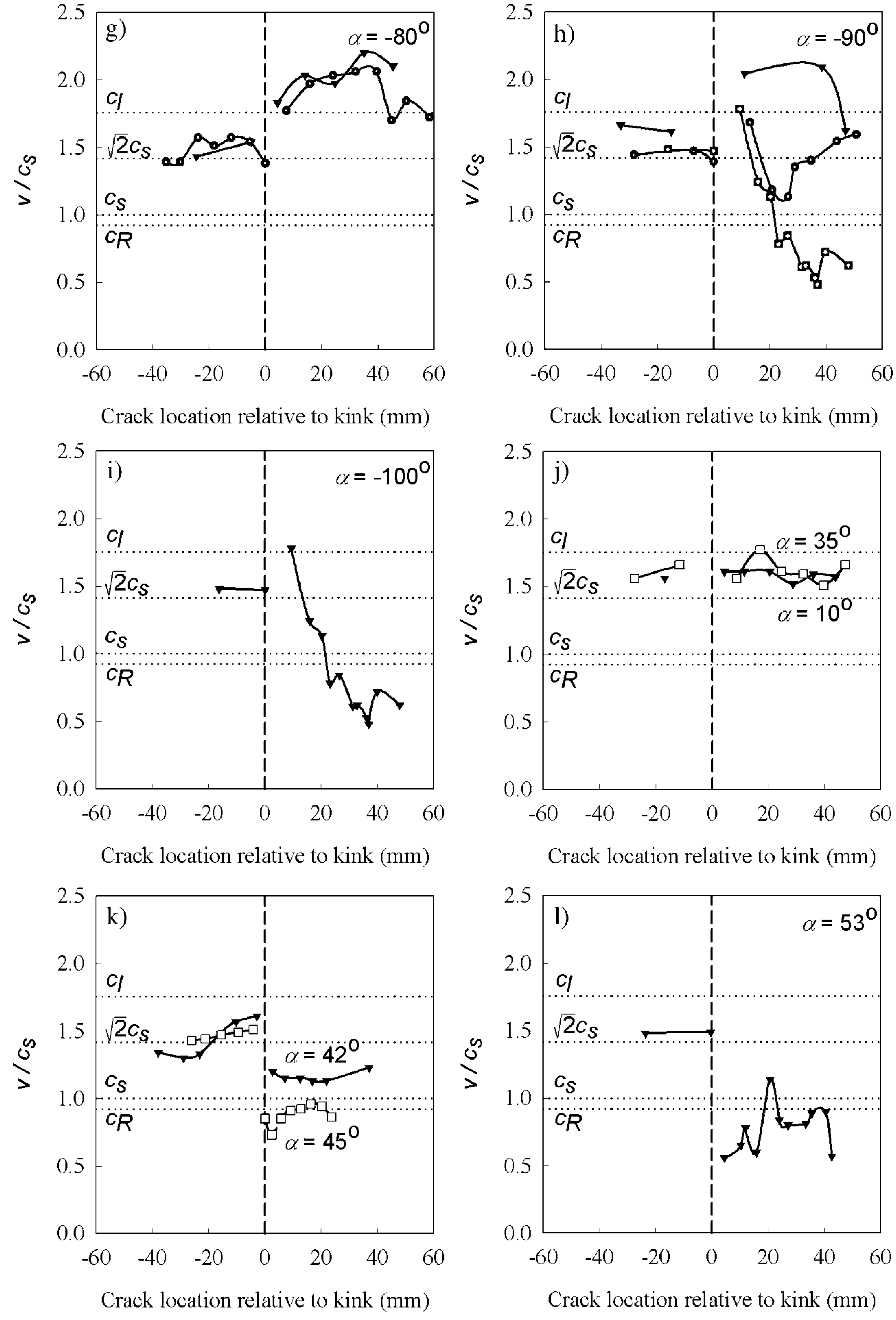

Figure 15. (continued)

the turn, reaching levels hovering in the vicinity of c_l (see Figures 15g and 15h). However, whereas the former remains at a relatively constant speed, the latter sustains irregular oscillations. Finally, the specimen with the backward incline angle of $-100°$ experiences an initial crack speed jump similar to those of the two specimens just cited but is unable to maintain high speed levels, dropping to below c_R (Figure 15i).

[58] On the compressional side, the behavior of cracks along shallow angles ($\alpha = 10°, 35°$) is almost indistinguishable from that of their tensile counterparts (see Figure 15j). The inability of the 22.5° Karadere bend of the North Anatolian fault to substantially slow down the intersonically moving East bound rupture of the 1999 Izmit earthquake [*Harris et al.*, 2002] is consistent with the above observation. Larger incline angles of 42°, 45° (Figure 15k), and 53° (Figure 15l) show even more severe drops in speed with increasing angles to very low subsonic values. Beyond 53°, the crack is incapable of further motion along the incline. Also, starting with the specimen having the incline angle of 42°, upon reaching the end of the primary plane, the crack elects to follow the incline while simultaneously branching into the bulk material. The speed of the mode-I branched crack seems to increase with increasing angle of the weakened secondary path, gradually changing from 0.25 c_R to 0.5 c_R.

[59] The most relevant information from these numerous tests consists in the speeds immediately following the crack turn onto the secondary plane. This data is captured and summarized in Figure 16a, normalized with respect to c_s. For secondary paths inclined toward the extensional side, there is a steady decline from 0° to $-56°$, from the range $\sqrt{2}c_s < v < c_l$ to a level between $c_s < v < \sqrt{2}c_s$, after which point an increase takes the crack speed to levels nearing c_l at $-90°$. On the compressional side, the crack speed remains fairly constant up to 35°, then drops drastically to zero near 60°.

[60] Referring back to Figure 14, a local maximum value of shear stress occurs for $\theta = 0°$, with no associated normal stress present. It is expected, therefore, that this straight path would be preferential for crack propagation under the present loading condition when compared to possible adjoining paths. As the crack encounters alternate weak planes of large angular orientation, conditions prevailing at the crack tip, corresponding to the direction of the provided incline, will come into play. In addition to the effect of $\sigma_{r\theta}$, the circumferential stress, $\sigma_{\theta\theta}$, would open a path to the incoming crack, if tensile, thereby facilitating and perhaps even expediting a jump onto the secondary plane. If compressive, the effect of $\sigma_{\theta\theta}$ would be that of sealing the secondary plane further. The practical effect of this is one of a virtually strengthened bond (frictional strengthening) offering even more resistance to crack penetration and continuing motion. In light of this discussion, particular attention should be paid to three distinct angular segments. First, notice the region of $-121° < \theta < -94°$, where the value of shear attains another local maximum that is even stronger than at $\theta = 0°$. Coupled with the fact that this is also a region of maximum tensile hoop stress, a prediction of enhanced crack continuation along secondary paths within the said zone can be advanced. Second, near $\theta = -56°$, no shear is manifest. Therefore conditions here can be surmised as being ominous to secondary crack motion. Finally, for all positive values of θ, compressive hoop stresses abound, and this should also discourage secondary crack propagation.

[61] Figure 16b attempts to capture the ease of penetration into a secondary plane. This can be achieved effectively in terms of the already visited postkink speeds. The effect of varying incoming crack speed is annulled by normalization of the postkink speeds with respect to that entity. In addition, it provides the requisite comparison of post- to prekink speed, thereby providing a ratio of secondary to primary energy expended into the crack. At shallow angles, say $-35° < \alpha < 35°$, the relative shear stress has dropped slightly with respect to its value at 0°, which is unity. Concurrently, a small amount of positive circumferential stress is present for negative kink angles, whereas negative hoop stresses of the same magnitude exist for positive kink angles. However, due to the relatively limited size of these stresses and the fact that the shear stress is still near a maximum level, little difference in behavior can be perceived between these opposite cases. Also, based on their speed history, neither can they be differentiated from an intersonic shear crack running self similarly and continuously along its original plane.

[62] As the negative kink angles of the secondary plane become more obtuse, the amount of shear available to potentially initiate a crack along that path decreases. At the same time, increasing circumferential stress allows for more mode-I opening, leading to mixed-mode conditions. At angle $\alpha = -56°$, with no more shear present, advance of a crack along that path is theoretically limited to c_R, thus the large drops in crack speed recorded experimentally in the vicinity of that angle. Increasing the kink angle further changes the sign of shear, resulting in an abrupt reversal in displacement direction between the two sections of the specimen. As the angle draws near $-90°$, the most favorable conditions for crack initiation along secondary paths are met. Indeed, the highest tensile, opening stress of any angle is attained, considerably weakening the effectiveness of the bond. Simultaneously, the shear stress reaches a value whose magnitude approaches the absolute maximum shear stress obtainable at any kink angle θ. This is reflected by the continuous escalation in crack speed, with increasing angle beyond $\alpha = -56°$, to levels exceeding unity. This culminates in the very high speed ratios obtained at $-80°$, $-90°$, and $-100°$. Propagation along the latter kink angle seems somewhat counterintuitive since upon reaching the intersection of the two paths, the crack must make a turn and move back in the direction from which it originally came, changing local slip direction from right-lateral to left-lateral slip. However, the solution does guarantee this outcome based on high-shear and high-tensile hoop stresses. Nevertheless, a slight drop is observed in the figure, when the data point at $\alpha = -100°$ is compared to those of the two previous kink angles. Though the crack speed drop appears miniscule, it is actually of considerable importance as it is indicative of a trend, since tests performed at $\alpha = -125°$ and higher resulted instead in crack penetration into the bulk of the material. Analysis of the crack-tip stress field does not exhibit any impediment to initiation along these obtuse paths, except for the constantly diminishing levels of both shear and tensile stress components to eventually zero at $-180°$.

[63] On the compressional side, the conditions for shallow angles are similar to those of negative angles of

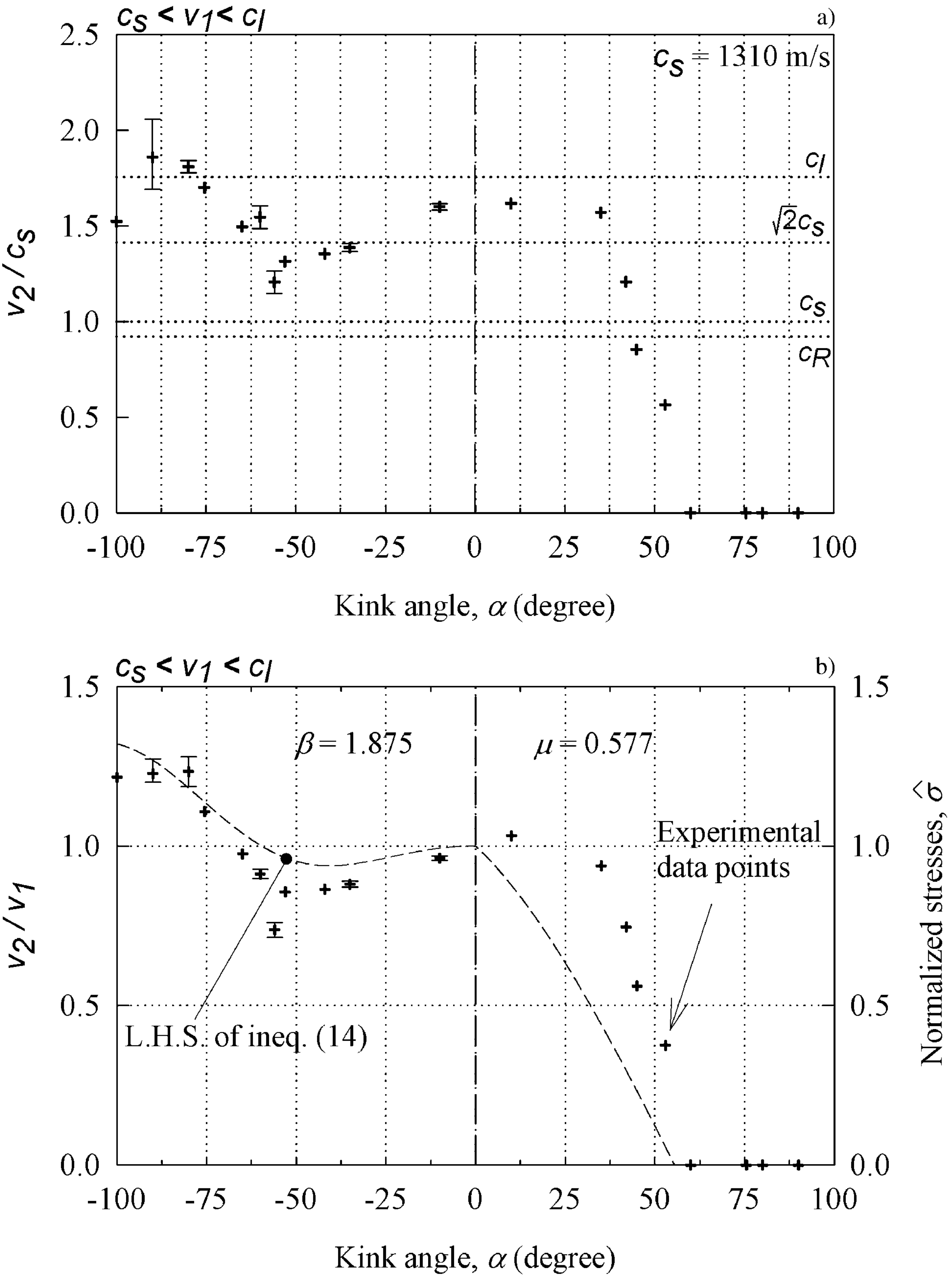

Figure 16. Crack speed along fault bends of various inclinations for incoming intersonic shear cracks. (a) Raw data. (b) The crack speed along the secondary fault normalized by the terminal crack speed of the primary plane. Theoretical predictions of the crack speed based on the intersonic crack-tip stress field are also plotted (broken line) as a function of fault inclination.

equivalent magnitude. Therefore ease to propagation is expected, as evidenced by the high-speed ratios observed in Figure 16b at $\alpha = 10°$ and 35°. As angular inclination is increased, shear stress drops. At the same time, compressive hoop stress increases and gradually frictionally enhances the effective bond strength, impeding crack motion. This is corroborated by the continuously decreasing crack speed recorded experimentally as kink angle increases. Near 56°, the shear stress declines to zero, while hoop stress is still highly compressive. Incline paths near that point can therefore no longer be triggered by the incoming crack. This is observed experimentally up to $\alpha = 90°$. Although near that point the shear stress has increased substantially, so has the compressive hoop stress, to the extent of preventing further motion along the incline.

[64] Thus far, qualitative analyses based on the crack-tip stress fields (equations (15)–(17)) have been used to understand the behavior of cracks as they enter an incline. However, quantitative measurements are necessary to better predict the relative incoming speeds onto the inclines. Inequality (14) is used for that purpose, in combination with the intersonic crack-tip stress fields. The expression is composed of two elements, one in which cohesion prevails and is valid only on the extensional side, and another which takes friction into account and is applicable only to the compressional side. Inequality (14) is plotted as a continuous curve with respect to angular inclination of the secondary plane and is superimposed on the experimental data points of Figure 16b. Note that the angular variations involved in the expression are automatically normalized in such a way as to predict a value of unity at $\theta = 0°$. The quantity $\hat{\sigma}(\alpha, v_1)$ represents a compound measure of crack driving force and fault resistance along $\theta = \alpha$ and is expected to correlate with postkink speed v_2. Indeed, within the experimental window, the angular trend between speed ratio and $\hat{\sigma}(\alpha, v_1)$ is remarkable. On the extensional side, the theoretical $\hat{\sigma}(\alpha, v_1)$ curve registers a gradual decline with increasing angle, up to $\theta = -45°$, followed by a rise that ends at $\theta = -100°$, at a level comparable to that of the actual experimentally measured crack speed of the same angular inclination. Larger values of the shear stress factor, β (say a 20% increase), ameliorate the match between the curve and the measured data points, as the level of the curve is lowered slightly to almost coincide with the experimental symbols. Such an increase in the value of β would not be unreasonable since it is well within the range of error associated with the experimental evaluation of σ_0 and τ_0. Furthermore, the minimum is shifted to the left, toward $\theta = -56°$, where the minimum is also registered experimentally. On the compressional side, where normalized stresses have been scaled to fit the range between zero and one, the theory bypasses the experimental plateau preceding the drop in crack speed with increasing angle. Instead, the decrease is immediate, ending with a value of zero at $\theta = 56°$, precisely where crack propagation along the inclines is no longer observed experimentally.

[65] Inequality (14) can also be used as a simple predictor of the ability of the crack to engage into an incline. The predicted value of $\hat{\sigma}(\alpha, v_1)$ is largely influenced by the value of the free parameters β and μ. On the compressional side, as the friction coefficient increases, the value of $\hat{\sigma}(\alpha, v_1)$ decreases because of the contribution of the term accounting for the frictional strengthening of the bond. As a result, the curves shift down and to the left, restricting the range of angles within which crack motion is allowed (Figure 17a). For the friction coefficient assumed in this study, $0.5 < \mu < 0.6$, incline angles beyond $\alpha = 35°$ would not permit crack growth along their paths. Crack motion along the bend, within the range $35° < \alpha < 60°$, does occur but is further complicated by the fact that the available energy must be shared with a simultaneously generated

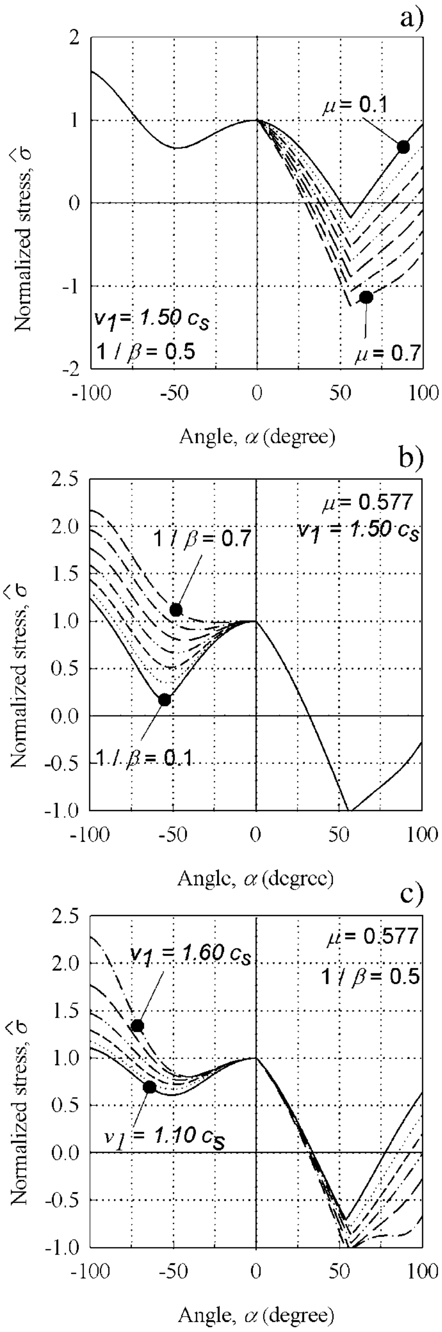

Figure 17. Variation of the normalized driving stress measure $\hat{\sigma}(\theta, v_1)$ (a) as a function of friction coefficient μ, (b) as a function of shear stress factor β, and (c) as a function of incoming rupture speed v_1.

tertiary mode-I crack which proceeds laboriously within the bulk of the material. This dual and intricate phenomenon cannot be captured by inequality (14), which within its defined parameters still delivers an excellent performance.

[66] On the extensional side, $\hat{\sigma}(\theta, v)$ is heavily influenced by the value of β. The left side of inequality (14) is parameterized and plotted for several values of $1/\beta$. As seen in Figure 17b, failure along the bend is forecasted everywhere within the experimental range for all values of the shear stress factor. However, as $1/\beta$ decreases, its minimum value shifts to the left, toward the experimentally registered incline angle that corresponds to the minimum crack speed.

[67] Finally, inequality (14) is plotted as a function of incline angles, for several values of the incoming speed v_1 (Figure 17c). The speed was varied at equal intervals, between 1.10 c_s and 1.60 c_s. Variation of $\hat{\sigma}(\theta, v)$ with incoming crack speed was not tested experimentally. Nevertheless, from the excellent correlation between inequality (14) and experimental data, it can be surmised that for any incline situated on the extensional side, as is observed in the figure, greater incoming speed will also result in greater outgoing speed along the secondary path. On the compressional side, the opposite happens, as the increase in crack-tip shear stress is simultaneously accompanied by even larger increase compressive stresses along the secondary path. However, in this case, the dependence on incoming speed is not so pronounced as on the extensional side. Nevertheless, increasing the incoming crack speed along the main path would result in smaller crack speed along the secondary path and would also decrease the range of secondary path angles allowing rupture continuation.

10. Conclusion

[68] Several experiments were conducted with the aim of duplicating conditions that may be present during crustal earthquake ruptures. Differences do exist, however, between the actual events and these laboratory earthquake simulations. In particular, static precompression is deliberately overlooked as these experiments are meant to uniquely isolate the influence of secondary fault bends on a running rupture. Both subsonic and intersonic incoming ruptures are investigated as earthquake ruptures are believed to have the capability of propagating in both regimes. In the subsonic case, criteria based on energy and on the asymptotic elastodynamic crack-tip stress field are effectively used to explain experimental observations. Only the latter approach is valid in the intersonic regime and is used successfully to predict the behavior of ruptures as they reach the intersection of two planar faults. Finally, it is worth noting that the secondary tensile microcracks that appear on the extensional side of the shear rupture faces are thought to be common to both events, suggesting that a dynamic fracture mechanics approach and bonded interfaces adequately mimic conditions present along earthquake faults.

[69] **Acknowledgments.** The authors would like to acknowledge the support of the Office of Naval Research (Ship Structures Program), grant N00014-95-1-0453, as well as the support of the National Science Foundation (Geophysical Sciences Directorate) through grant EAR-0207873. Many helpful discussions with James Rice and Renata Dmowska of Harvard University, Hiroo Kanamori of Caltech, and Ruth Harris of the U.S. Geological Survey are also acknowledged.

References

Abraham, F. F., and H. J. Gao, How fast can cracks propagate?, *Phys. Rev. Lett.*, *84*(14), 3113–3116, 2000.

Aochi, H., R. Madariaga, and E. Fukuyama, Effect of normal stresses during rupture propagation along nonplanar faults, *J. Geophys. Res.*, *107*(B2), 2038, doi:10.1029/2002JB000500, 2002.

Archuleta, R. J., A faulting model for the 1979 Imperial Valley earthquake, *J. Geophys. Res.*, *89*(6), 4559–4585, 1984.

Bouchon, M., M.-P. Bouin, H. Karabulut, M. N. Toksöz, M. Dietrich, and A. J. Rosakis, How fast is rupture during an earthquake? New insights from the 1999 Turkey earthquakes, *Geophys. Res. Lett.*, *28*(14), 2723–2726, 2001.

Broberg, K. B., *Cracks and Fracture*, Academic, San Diego, Calif., 1999.

Burridge, R., G. Conn, and L. B. Freund, The stability of a rapid mode II crack with finite cohesive traction, *J. Geophys. Res.*, *84*(B5), 2210–2222, 1979.

Camacho, G. T., and M. Ortiz, Computational modeling of impact damage in brittle materials, *Int. J. Solids Struct.*, *33*(20–22), 2899–2938, 1996.

Cotterell, B., and J. R. Rice, Slightly curved or kinked cracks, *Int. J. Fract.*, *16*, 155–169, 1980.

Das, S., Application of dynamic shear crack models to the study of the earthquake faulting process, *Int. J. Fract.*, *27*, 263–276, 1985.

Freund, L. B., The mechanics of dynamic shear crack propagation, *J. Geophys. Res.*, *84*(B5), 2199–2209, 1979.

Freund, L. B., *Dynamic Fracture Mechanics*, Cambridge Univ. Press, New York, 1990.

Gao, H. J., Y. G. Huang, P. Gumbsch, and A. J. Rosakis, On radiation-free transonic motion of cracks and dislocations, *J. Mech. Phys. Solids*, *47*, 1941–1961, 1999.

Harris, R. A., J. F. Dolan, R. Hartleb, and S. M. Day, The 1999 Izmit, Turkey, earthquake: A 3D dynamic stress transfer model of intraearthquake triggering, *Bull. Seismol. Soc. Am.*, *92*, 245–255, 2002.

Kame, N., J. R. Rice, and R. Dmowska, Effects of prestress state and rupture velocity on dynamic fault branching, *J. Geophys. Res.*, *108*(B5), 2265, doi:10.1029/2002JB002189, 2003.

Kanamori, H., Mechanics of earthquakes, *Annu. Rev. Earth Planet. Sci.*, *22*, 207–237, 1994.

King, G. C. P., and J. L. Nabelek, Role of fault bends in the initiation and termination of rupture, *Science*, *228*, 984–987, 1985.

Lambros, J., and A. J. Rosakis, Development of a dynamic decohesion criterion for subsonic fracture of the interface between two dissimilar materials, *Proc. R. Soc. London*, *451*, 711–736, 1995.

Needleman, A., Analysis of intersonic crack growth under shear loading, *J. Appl. Mech.*, *66*(4), 847–857, 1999.

Olsen, K. B., R. Madariaga, and R. J. Archuleta, Three-dimensional dynamic simulation of the 1992 Landers earthquake, *Science*, *278*, 834–838, 1997.

Poliakov, A. N. B., R. Dmowska, and J. R. Rice, Dynamic shear rupture interactions with fault bends and off-axis secondary faulting, *J. Geophys. Res.*, *107*(B11), 2295, doi:10.1029/2001JB000572, 2002.

Ramulu, M., and A. S. Kobayashi, Mechanics of crack curving and branching—A dynamic fracture analysis, *Int. J. Fract.*, *27*(3–4), 187–201, 1985.

Rice, J. R., New perspectives on crack and fault dynamics, in *Proceedings of the 20th International Congress of Theoretical and Applied Mechanics, Mechanics for a New Millennium*, pp. 1–23, Kluwer Acad., Norwell, Mass., 2001.

Rosakis, A. J., Intersonic shear cracks and fault ruptures, *Adv. Phys.*, *51*(4), 1189–1257, 2002.

Rosakis, A. J., O. Samudrala, and D. Coker, Cracks faster than the shear wave speed, *Science*, *284*, 1337–1340, 1999.

Samudrala, O., Y. Y. Huang, and A. J. Rosakis, Subsonic and intersonic mode II crack propagation with a rate-dependent cohesive zone, *J. Mech. Phys. Solids*, *50*, 1231–1268, 2002a.

Samudrala, O., Y. Huang, and A. J. Rosakis, Subsonic and intersonic shear rupture of weak planes with a velocity weakening cohesive zone, *J. Geophys. Res.*, *107*(B8), 2170, doi:10.1029/2001JB000460, 2002b.

Segall, P., and Y. Du, How similar were the 1934 and 1966 Parkfield earthquakes?, *J. Geophys. Res.*, *98*, 4527–4538, 1993.

Singh, R. P., J. Lambros, A. Shukla, and A. J. Rosakis, Investigation of the mechanics of intersonic crack propagation along a bimaterial interface using coherent gradient sensing and photoelasticity, *Proc. R. Soc. London, Ser. A*, *453*(1967), 2649–2667, 1997.

Xu, L. R., Y. Y. Huang, and A. J. Rosakis, Dynamic crack deflection and penetration at interfaces in homogeneous materials: Experimental studies and model predictions, *J. Mech. Phys. Solids*, *51*, 461–486, 2003.

A. J. Rosakis, Graduate Aeronautical Laboratories, California Institute of Technology, Pasadena, CA 91125, USA. (rosakis@atlantis.caltech.edu)

C.-E. Rousseau, Department of Mechanical Engineering, University of Rhode Island, 222B Wales Hall, Kingston, RI 02881, USA. (rousseau@egr.uri.edu)